

Vortex-bound solitons in topological superfluid ^3He

J. T. Mäkinen¹, K. Zhang^{1,2,3}, and V. B. Eltsov¹

¹ Department of Applied Physics, Aalto University, FI-00076 Aalto, Finland

² Department of Physics and Helsinki Institute of Physics, P.O. Box 64, FI-00014 University of Helsinki, Finland

³ Department of Physics and Astronomy, University of Sussex, Falmer, Brighton BN1 9QH, United Kingdom

E-mail: vladimir.eltsov@aalto.fi

Abstract. The different superfluid phases of ^3He break several symmetries. The resulting p -wave order parameters include anisotropy axes both in the orbital and spin spaces, characterizing those broken symmetries. The free energy has several degenerate minima for certain orientations of anisotropy axes and spatial variation of the order parameter between two such regions, settled in different energy minima, forms a topological soliton. Such solitons can terminate in the bulk liquid, where the termination line forms a vortex with trapped circulation of mass and spin superfluid currents. We discuss possible soliton-vortex structures based on the symmetry and topology arguments and focus on the three structures observed in the experiments: solitons bounded by spin-mass vortices in the B phase, solitons bounded by half-quantum vortices in the polar and polar-distorted A phases, and composite defect of the soliton and the Kibble-Lazarides-Shafi wall in the polar-distorted B phase. The observations are based on nuclear magnetic resonance (NMR) techniques and are of three types: soliton can form a potential well for trapped spin waves, observed as an extra peak in the NMR spectrum; soliton can increase relaxation rate of the NMR spin precession; and the soliton can present the boundary conditions for the anisotropy axes in bulk and thus modify the bulk NMR signal. Thanks to the prominent NMR signature and the ability to manipulate the soliton structure with external magnetic field, solitons have become an important tool for probing and controlling the structure and dynamics of superfluid ^3He , in particular half-quantum vortices with core-bound Majorana modes.

1. Introduction

1.1. Superfluidity in bulk ^3He

At temperatures well below the Fermi temperature $T_F \sim 1$ K but above the superfluid transition temperature $T_c \sim 1$ mK, ^3He behaves as Fermi liquid, as described by Landau [1]. Properties of the Fermi liquid can be modeled through a weakly interacting gas of excitations in the vicinity of the Fermi surface. These excitations come in two flavors, as they may either be particle-like with $|p| > p_F$, where p_F is the Fermi momentum, or hole-like with $|p| < p_F$. According to the Bardeen-Cooper-Schrieffer (BCS) theory

[2], the presence of any attractive interaction, in the case of ${}^3\text{He}$ arising from Van der Waals interaction accompanied by spin-fluctuation exchange mechanism [3], there exists a temperature below which the fermions tend to form a coherent macroscopic condensate via formation of Cooper pairs. The spin-exchange mechanism favors p -wave pairing with angular momentum $l = 1$. Simultaneously, the antisymmetry of the fermionic wave function requires $s = 1$, where s is the spin quantum number for the Cooper pair.

The formation of Cooper pairs becomes energetically favorable below the critical temperature T_c , and the liquid undergoes a phase transition to the superfluid state. Above the superfluid transition bulk ${}^3\text{He}$ is described by the symmetry group [4]

$$G = SO(3)_{\mathbf{L}} \times SO(3)_{\mathbf{S}} \times U(1)_{\phi} \times T \times C \times P, \quad (1)$$

which includes continuous symmetries, three-dimensional rotations of coordinates $SO(3)_{\mathbf{L}}$, rotations of the spin space $SO(3)_{\mathbf{S}}$, and the global phase transformation group $U(1)_{\phi}$, as well as discrete symmetries, T is the time-reversal symmetry, C is the particle-hole conversion symmetry, and P is the space parity symmetry. The transitions from normal fluid to superfluid phases as well as transitions between different superfluid phases are accompanied by spontaneous breaking of continuous and/or discrete symmetries in G . In bulk ${}^3\text{He}$ three superfluid phases have been realized [3], Fig. 1; the fully-gapped superfluid B phase characterized by broken relative spin-orbit symmetry, the chiral $p_x + ip_y$ superfluid A phase, and finally, the spin-polarized A_1 phase close to T_c in high magnetic fields.

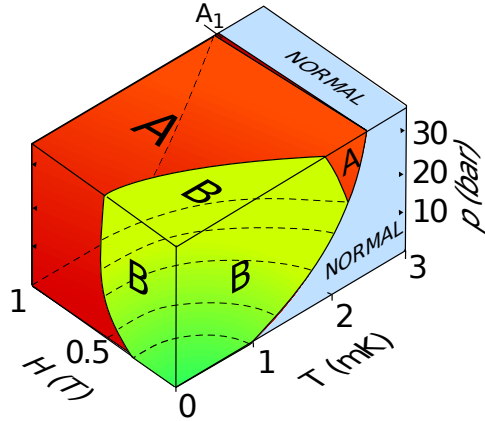


Figure 1. Superfluid phase diagram of bulk ${}^3\text{He}$. At 1 bar pressure ${}^3\text{He}$ liquefies at ~ 3.2 K. It remains liquid all the way to the absolute zero temperature for pressures $P \lesssim 30$ bar. In bulk fluid, three different superfluid phases are observed below the critical temperature – the time-reversal symmetric B phase, the chiral equal spin-pairing A phase, and at high magnetic fields the A_1 phase which only allows Cooper pairs with both spins oriented along the magnetic field.

2. Residual symmetries in superfluid phases

Soliton is formed by continuous variation of the order parameter between two regions which settle in distinct but energetically degenerate states. Within the soliton the free energy is not at minimum, but the winding of the order parameter is topologically protected with the π_1 homotopy group [5]. This will be discussed in details later in the paper. Here we note that superfluid ^3He provides plenty of possibilities for existence of distinct but energetically degenerate states. In this section we review the symmetry classification of different superfluid phases of ^3He , both for bulk fluid and for fluid confined by nanostructured nematic aerogel. The residual symmetries are intimately linked to the existence of degenerate states.

2.1. Superfluid phases in bulk liquid

2.1.1. B phase In the absence of magnetic field the superfluid B phase has the total angular momentum $\mathbf{j} = \mathbf{l} + \mathbf{s} = 0$. The requirement $\mathbf{j} = 0$ allows three spin-configurations for Cooper pairs, i.e. $s_z = \{-1, 0, 1\}$ and, respectively, $l_z = \{1, 0, -1\}$. The B phase is characterized by broken spin-orbit symmetry, i.e. the relative orientation of the spin- and orbital vectors becomes locked. It is reflected in the order parameter of the B phase [3]

$$A_{\mu j}^{\text{B}} = \Delta_{\text{B}} e^{i\phi} \mathbf{R}_{\mu j}(\hat{\mathbf{n}}, \theta), \quad (2)$$

where Δ_{B} is the pressure- and temperature-dependent superfluid gap characterizing the energy required to break a Cooper pair, ϕ is the superfluid phase, and matrix $\mathbf{R}(\hat{\mathbf{n}}, \theta)$ describes the rotation of spins with index μ relative to the orbital coordinates with index j around the vector $\hat{\mathbf{n}}$ by angle θ . In equilibrium the spin-vector $\hat{\mathbf{s}}$ can be obtained from the orbital vector $\hat{\mathbf{l}}$ by rotating $\hat{\mathbf{l}}$ around axis $\hat{\mathbf{n}}$ by the ‘‘Leggett angle’’ $\theta = \arcsin(-1/4) \approx 104^\circ$, minimizing the spin-orbit interaction [6].

Taking into account the broken relative symmetry between the spin and orbital parts of the order parameter and the broken phase symmetry, the remaining symmetry in the B phase is [3, 4]

$$H_{\text{B}} = SO(3)_{\text{J}} \times T \times C \times PU_{\pi}, \quad (3)$$

where $SO(3)_{\text{J}}$ denotes the joint three-dimensional rotation in the orbital and spin spaces, and PU_{π} denotes the joint discrete symmetry of the parity P and π phase rotation U_{π} .

2.1.2. A phase The A phase is an equal-spin-pairing state, where the Cooper pairs consist of spins with the same sign and thus $s_z = \{-1, 1\}$. The order parameter of the A phase can be written as

$$A_{\mu j}^{\text{A}} = \Delta_{\text{A}} e^{i\phi} \hat{\mathbf{d}}_{\mu}(\hat{\mathbf{m}}_j + i\hat{\mathbf{n}}_j), \quad (4)$$

where the vectors $\hat{\mathbf{m}}$ and $\hat{\mathbf{n}}$ (different from the $\hat{\mathbf{n}}$ vector in the B phase) form an orthogonal triad with the Cooper pair orbital angular momentum axis $\hat{\mathbf{l}} = \hat{\mathbf{m}} \times \hat{\mathbf{n}}$,

$\hat{\mathbf{d}}$ is the spin anisotropy vector along which the total spin of a Cooper pair vanishes, and Δ_A is the maximum superfluid gap in the A phase. In the A phase, the gauge symmetry $U(1)_\phi$ is broken and any change of the order parameter phase $\phi \rightarrow \phi + \Delta\phi$ may be compensated by rotating the orbital component of the order parameter about $\hat{\mathbf{I}}$ by an angle $-\Delta\phi$, leaving the order parameter invariant under that particular combination of transformations. This combination corresponds to a remaining relative $U(1)_{\phi+\mathbf{L}}$ symmetry. Additionally, rotation of the spin space about vector $\hat{\mathbf{d}}$ leaves the order parameter unchanged, corresponding to a remaining $SO(2)_{\mathbf{S}}$ symmetry. The order parameter is also symmetric under the simultaneous rotation about perpendicular axis and π phase change, i.e. under transformation $(\hat{\mathbf{d}}, \phi) \rightarrow (-\hat{\mathbf{d}}, \phi + \pi)$, corresponding to a discrete symmetry described by the cyclic group \mathbb{Z}_2 (denoted $\mathbb{Z}_{2(\phi+\mathbf{S})}$) of order 2. In the A phase the time-reversal symmetry is partially broken due to the non-zero imaginary part in the orbital space, reducing it to the combined discrete symmetry $\mathbb{Z}_{2(T+\mathbf{L})}$ corresponding to simultaneous time reversal and π -rotation of the orbital space about $\hat{\mathbf{m}}$. The remaining symmetries are described by the group [3]

$$H_A = U(1)_{\phi+\mathbf{L}} \times \tilde{D}_{\infty\mathbf{S}} \times \mathbb{Z}_{2(T+\mathbf{L})} \times C \times PU_\pi, \quad (5)$$

where we have combined the symmetries $\tilde{D}_{\infty\mathbf{S}} \hat{=} SO(2)_{\mathbf{S}} \times \mathbb{Z}_{2(\phi+\mathbf{S})}$.

2.1.3. A₁ phase The last superfluid phase encountered in bulk fluid, the A₁ phase, exists only at a very narrow temperature region close to T_c , in the presence of magnetic field. The A₁ phase consists of Cooper pairs with both spins oriented along the direction of the magnetic field. The order parameter of the A₁ phase can be written as

$$A_{\mu j}^{A_1} = \Delta_{A_1} e^{i\phi} (\hat{\mathbf{d}}_\mu + i\hat{\mathbf{e}}_\mu)(\hat{\mathbf{m}}_j + i\hat{\mathbf{n}}_j), \quad (6)$$

where $\hat{\mathbf{d}}$ and $\hat{\mathbf{e}}$ form an orthogonal triad in spin space with vector $\hat{\mathbf{f}} = \hat{\mathbf{d}} \times \hat{\mathbf{e}}$ and Δ_{A_1} is the maximum gap in the A₁ phase. Similar to the A phase, a gauge transformation $A_{\mu j}^{A_1} \rightarrow e^{i\Delta\phi} A_{\mu j}^{A_1}$ can be compensated by simultaneous rotation of the orbital space by $-\Delta\phi$ about $\hat{\mathbf{I}}$, corresponding to remaining $U(1)_{\phi+\mathbf{L}}$ symmetry. On the other hand, the spin part of the order parameter has identical structure to the orbital part, and the gauge transformation can be compensated also by rotation of the spin space around $\hat{\mathbf{f}}$ by $-\Delta\phi$, resulting in a conserved $U(1)_{\phi+\mathbf{S}}$ corresponding to simultaneous rotation of the spin space and change of phase. Alternatively, one of the $U(1)$ symmetries may be interpreted as a simultaneous rotation of the orbital and spin spaces. Additionally, the time-reversal symmetry is partially broken due to the non-zero imaginary part both in orbital and spin spaces, reducing it to the combined discrete symmetry $\mathbb{Z}_{2(T+\mathbf{J})}$ corresponding to simultaneous time reversal, π -rotation of the orbital space about $\hat{\mathbf{m}}$, and π rotation of the spin space about $\hat{\mathbf{d}}$. Thus, the order parameter of the A₁ phase is invariant under [3]

$$H_{A_1} = U(1)_{\phi+\mathbf{L}} \times U(1)_{\phi+\mathbf{S}} \times \mathbb{Z}_{2(T+\mathbf{J})} \times C \times PU_\pi. \quad (7)$$

2.2. ^3He under confinement by nafen

The presence of nanostructured confinement, i.e. thin slabs [7, 8] or various aerogels [9, 10, 11, 12, 13], modify the superfluid phase diagram. Anisotropic confinement may also alter the symmetry group of the normal phase of ^3He by explicitly breaking the three-dimensional rotational symmetry in the coordinate space. Here we consider the effect of commercially available nematically ordered material called nafen [11], which breaks the three-dimensional continuous rotational symmetry $SO(3)_{\mathbf{L}}$ in Eq. (1). The total symmetry group of the normal phase is reduced to [4]

$$G' = D_{\infty\mathbf{L}} \times SO(3)_{\mathbf{S}} \times U(1)_{\phi} \times T \times C \times P, \quad (8)$$

where $D_{\infty\mathbf{L}}$ contains rotations about the nafen anisotropy axis $\hat{\mathbf{z}}$ and π rotations about perpendicular axes. This symmetry may also be written as a product of rotations of the space around the anisotropy axis and reflection with respect to the perpendicular plane, i.e. $D_{\infty\mathbf{L}} \hat{=} SO(2)_{\mathbf{L}} \times \mathbb{Z}_{2\mathbf{L}}$.

The resulting phase diagram in nafen with 90 mg/cm^3 density [11] is shown in Fig. 2. There are notable differences to the bulk phase diagram; the critical temperature is suppressed by a few percent and, more importantly, novel superfluid phases – the polar, polar-distorted A (PdA), and polar-distorted B (PdB) phases - are observed. In all cases the superfluid gap becomes anisotropic due to the effect of the confinement. Schematic illustrations of the superfluid gap in these phases are shown in Fig. 3.

2.2.1. Polar phase The order parameter of the polar phase can be written as

$$A_{\mu j}^{\text{P}} = \Delta_{\text{P}} e^{i\phi} \hat{\mathbf{d}}_{\mu} \hat{\mathbf{m}}_j, \quad (9)$$

where Δ_{P} is the maximum superfluid gap in the polar phase. The order parameter is invariant with respect to rotations of the spin space about $\hat{\mathbf{d}}$ and rotations of the orbital space about $\hat{\mathbf{m}}$, as well as about combined rotations about perpendicular axes and π phase changes, i.e. about transformations $(\hat{\mathbf{d}}, \phi) \rightarrow (-\hat{\mathbf{d}}, \phi + \pi)$ and $(\hat{\mathbf{m}}, \phi) \rightarrow (-\hat{\mathbf{m}}, \phi + \pi)$. Similarly to other superfluid phases, the gauge symmetry $U(1)_{\phi}$ is broken in the transition. The group of remaining symmetries in the polar phase is

$$H_{\text{P}} = \tilde{D}_{\infty\mathbf{L}} \times \tilde{D}_{\infty\mathbf{S}} \times T \times C \times PU_{\pi}, \quad (10)$$

where $\tilde{D}_{\infty\mathbf{L}}$ and $\tilde{D}_{\infty\mathbf{S}}$ are the symmetries involving π rotations about axes transverse to $\hat{\mathbf{m}}$ or $\hat{\mathbf{d}}$ in the orbital and spin spaces, respectively, combined with a phase rotation by $e^{\pi i}$. We have used the shorthand notation $\tilde{D}_{\infty\mathbf{L}} \hat{=} SO(2)_{\mathbf{L}} \times \mathbb{Z}_{2(\phi+\mathbf{L})}$ and $\tilde{D}_{\infty\mathbf{S}} \hat{=} SO(2)_{\mathbf{S}} \times \mathbb{Z}_{2(\phi+\mathbf{S})}$. One can then calculate the vacuum manifold R_{P} from the residual symmetry group H_{P} by taking the quotient space of G' over H_{P} [3]

$$R_{\text{P}} = G'/H_{\text{P}} = (S_{\mathbf{S}}^2 \times U(1))/\mathbb{Z}_{2(\phi+\mathbf{S})}, \quad (11)$$

where $S_{\mathbf{S}}^2$ is the 2-sphere.

It is interesting that despite strong scattering by the confining strands, the polar phase demonstrates very small suppression of the critical temperature compared to the bulk T_c . The robustness is provided by extension of the Anderson theorem, which can

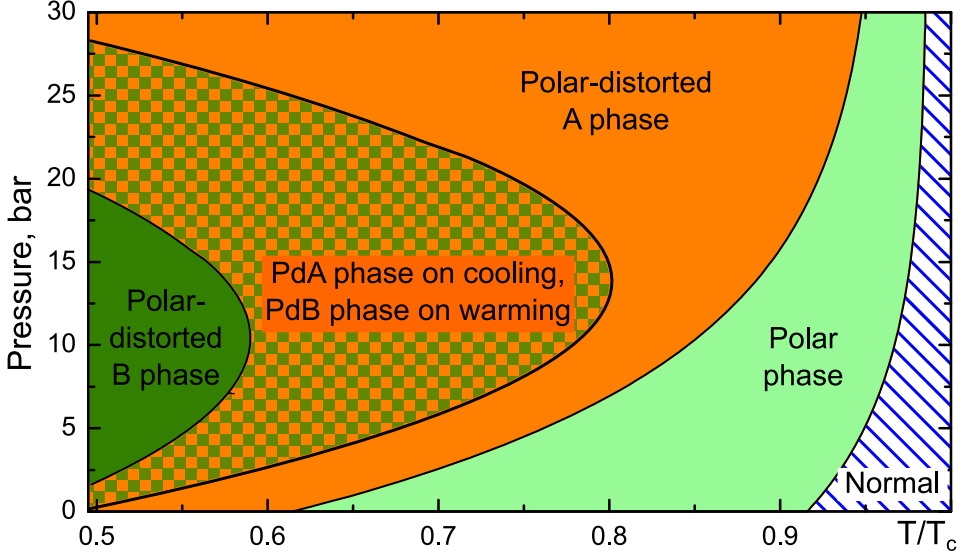


Figure 2. Superfluid phase diagram of ^3He under confinement by nafen. Nanostructured confinement by uniaxial cylinders modifies the symmetries of ^3He in the normal fluid and below the superfluid transition temperature. The superfluid transition with the highest critical temperature under these conditions occurs to the polar phase [11]. The phase diagram shown in this figure sketches the measured phase diagram in a sample of nematically ordered aerogel called nafen-90, which consists of nearly uniaxial strands of Al_2O_3 with density 90 mg/cm^3 . In addition to the polar phase, polar-distorted A (PdA) and polar-distorted B (PdB) phases are encountered at lower temperatures. The PdA phase can be supercooled, as illustrated by the patterned area.

be derived in case of p -wave pairing for the specular scattering from parallel strands [14, 15]. This robustness is also demonstrated by the characteristic T^3 low-temperature dependence of the gap resulting from the presence of the nodal line [15]. In realistic samples scattering is never completely specular, nor are the strands perfectly aligned, and a small suppression of T_c is thus observed.

2.2.2. Polar-distorted A phase In the 90 mg/cm^3 nafen sample, the polar-distorted A (PdA) phase is reached on cooling via a second-order phase transition from the polar phase [11]. The order parameter of the PdA phase is

$$A_{\mu j}^{\text{PdA}} = \Delta_{\text{PdA}} e^{i\phi} \hat{\mathbf{d}}_{\mu} (\hat{\mathbf{m}}_j + ib\hat{\mathbf{n}}_j), \quad (12)$$

where $0 < b < 1$ is a dimensionless parameter characterizing the gap distortion and $\Delta_{\text{PdA}}(b)$ is the maximum gap in the PdA phase. For $b = 0$ the order parameter of the polar phase is obtained, while $b = 1$ recovers the order parameter of the bulk A phase. The order parameter is symmetric under rotations of the spin space about $\hat{\mathbf{d}}$, about the combined transformation $\mathbb{Z}_{2(\phi+\mathbf{s})}$, and about π rotation about $\hat{\mathbf{l}}$ and π phase change, i.e. about $(\hat{\mathbf{m}}, \hat{\mathbf{n}}, \phi) \rightarrow (-\hat{\mathbf{m}}, -\hat{\mathbf{n}}, \phi + \pi)$. Moreover, the $\tilde{D}_{\infty\mathbf{s}}$ symmetry is preserved in the polar-PdA transition due to similar spin structure of the order parameter. In the orbital space π rotations about the axis $\hat{\mathbf{l}}$, in combination with a phase rotation $e^{\pi i}$,

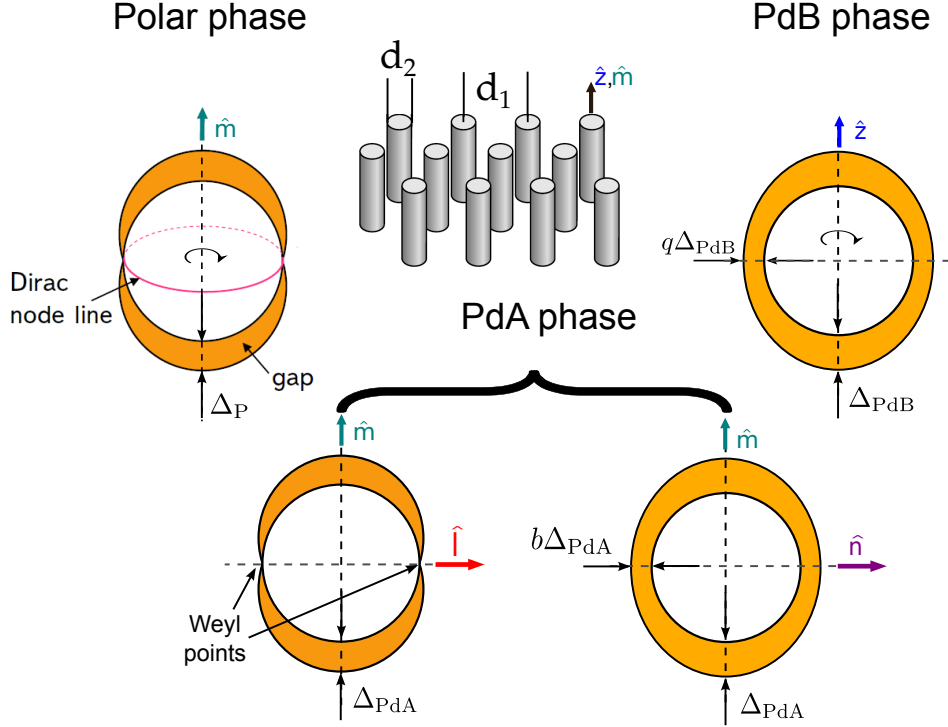


Figure 3. Schematic illustration of superfluid gaps in superfluid phases presented in Fig. 2. The polar phase and PdB phase gaps are symmetric under rotation by the nafen axis, and the PdA phase gap is shown in two projections as it lacks the rotational symmetry. For each phase, the maximum gap is oriented along the anisotropy axis of nafen strands, which have characteristic diameter $d_1 \approx 9$ nm and separation $d_2 \sim 50$ nm. Gap asymmetry is drawn not to scale.

form a symmetry, i.e. the orbital symmetry is reduced to a discrete symmetry $\mathbb{Z}_{2(\phi+\mathbf{L})}$. Similar to the bulk A phase, the time-reversal symmetry is partially broken in the PdA phase and the PdA phase is invariant under the combined discrete symmetry $\mathbb{Z}_{2(T+\mathbf{L})}$. The residual symmetry group in the PdA phase is

$$H_{\text{PdA}} = \mathbb{Z}_{2(\phi+\mathbf{L})} \times \tilde{D}_{\infty\mathbf{S}} \times \mathbb{Z}_{2(T+\mathbf{L})} \times C \times PU_{\pi}. \quad (13)$$

Assuming phase transition from the normal phase, the vacuum manifold of the PdA phase becomes

$$R_1^{\text{PdA}} = G'/H_{\text{PdA}} = SO(2)_{T+\mathbf{L}} \times S_{\mathbf{S}}^2 \times U(1). \quad (14)$$

In addition, the group H_{PdA} is also the subgroup of H_{P} , reflecting the fact that the PdA-polar phase transition is of the second order. For the polar-PdA transition, the vacuum manifold becomes

$$R_2^{\text{PdA}} = H_{\text{P}}/H_{\text{PdA}} = SO(2)_{T+\mathbf{L}}. \quad (15)$$

It is worth underlining that the PdA phase can be reached via two routes involving only second order phase transitions, described by the vacuum manifolds (14) and (15). The consequences will be discussed in Sec. 2.2.4.

2.2.3. Polar-distorted B phase Depending on the confinement, the phase transition to the polar-distorted B phase (PdB) may occur directly from the normal phase [16], via a first-order transition from the PdA phase [11] (as realized in the nafen-90 sample), or, in principle, via a second-order phase transition from the polar phase. The order parameter of the PdB phase in zero magnetic field can be written as

$$A_{\mu j}^{\text{PdB}} = \Delta_{\text{PdB}} e^{i\phi} (\hat{\mathbf{d}}_{\mu} \hat{\mathbf{z}}_j + q_1 \hat{\mathbf{e}}_{\mu}^1 \hat{\mathbf{x}}_j + q_2 \hat{\mathbf{e}}_{\mu}^2 \hat{\mathbf{y}}_j), \quad (16)$$

where $|q_1| = |q_2| \equiv q \in (0, 1)$ describes the relative gap size in the plane perpendicular to the strands. Vectors $\hat{\mathbf{e}}^1$ and $\hat{\mathbf{e}}^2$ are unit vectors in the spin space and form an orthogonal triad with vector $\hat{\mathbf{d}}$. The maximum gap $\Delta_{\text{PdB}}(q)$ is achieved along the nafen anisotropy axis $\hat{\mathbf{z}}$. For $q = 0$, the order parameter of the polar phase is obtained while $q = 1$ recovers the order parameter of the bulk B phase. The order parameter is symmetric under the joint rotation of the spin and orbital spaces about the nafen anisotropy axis $\hat{\mathbf{z}}$. The remaining symmetries in the PdB phase are

$$H_{\text{PdB}} = SO(2)_{\mathbf{J}} \times T \times C \times PU_{\pi}, \quad (17)$$

where the subscript notation \mathbf{J} refers to the symmetry of the simultaneous rotation of orbital and spin spaces.

The vacuum manifold for the normal-PdB phase is obtained from

$$R_1^{\text{PdB}} = G'/H_{\text{PdB}} = SO(3)_{\mathbf{J}} \times U(1). \quad (18)$$

The group H_{PdB} is again a subgroup of H_{P} , reflecting the fact that also the polar-PdB phase transition is of second order. In this case, the resulting vacuum manifold becomes

$$R_2^{\text{PdB}} = H_{\text{P}}/H_{\text{PdB}} = SO(2)_{\mathbf{J}} \times \mathbb{Z}_{2(\phi+\mathbf{s})}. \quad (19)$$

We note that R_2^{PdB} is a disconnected space characterized by states $(\mathbf{d}, \mathbf{e}^1, \mathbf{e}^2, \phi)$ and $(-\mathbf{d}, -\mathbf{e}^1, \mathbf{e}^2, \pi + \phi)$. These spaces can not be made equal by any action from H_{P} . Moreover, calculating $\pi_0(R_2^{\text{PdB}})$ yields $\mathbb{Z}_{2(\mathbf{s}+\phi)}$, which describes a domain wall structure. This is in contrast to π_1 homotopy group which describe solitons. As we will see later, this domain wall combines with multiple possible soliton structures into composite topological defects.

2.2.4. Symmetry breaking patterns and fibrations of vacuum manifolds Besides stabilizing novel superfluid phases, confinement by nafen features even more complicated symmetry breaking patterns not possible in bulk samples. Such symmetry-breaking phase transitions can be used to study cosmological and dark matter models with spontaneous symmetry breaking (SSB) [17, 18, 19, 20, 21, 22, 23, 24] and, in particular, topological defects that appear in such theories. In nafen samples, the following symmetry breaking pattern

$$\begin{array}{ccccccc} G' & \longrightarrow & H_{\text{P}} & \subset & G' & \longrightarrow & H_{\text{PdA}} \subset H_{\text{P}} \subset G' \\ & & & & & \searrow & \updownarrow \\ & & & & & & H_{\text{PdB}} \subset H_{\text{P}} \subset G' \end{array} \quad (20)$$

can in principle be realized, where solid arrows represent the directions of symmetry reduction through SSB, and the dashed line represents the first order transition.

The SSB pattern, Eq. (20), suggests that, starting from the normal phase, both the PdA and PdB phases are accessible via two consecutive second-order steps. Denoting the vacuum manifolds generated through SSB from normal phase as

$$R_{\text{P}} = G'/H_{\text{P}}, R_1 = G'/H_{(\text{PdA/PdB})}, \quad (21)$$

and the vacuum manifolds accessible via the polar phase as

$$R_2 = H_{\text{P}}/H_{(\text{PdA/PdB})} \quad (22)$$

we find $R_2 \subset R_1$. Applying the third isomorphism theorem $R_1/R_2 = (G'/H_{\text{PdB}})/(H_{\text{P}}/H_{\text{PdB}})$ [25], we get

$$R_1/R_2 \cong R_{\text{P}} = G'/H_{\text{P}}. \quad (23)$$

Eq. (23) suggests that the normal phase vacuum manifolds R_1 consists of infinite disjoint subspaces (cosets) R_2^r , which relate to R_2 through action of $r \in R_1$ i.e., $R_2^r = rR_2$. We also notice that every R_2^r is isomorphically mapped to an element of the vacuum manifold of the polar phase. Mathematically speaking, this signifies that the vacuum manifold R_1 covers R_{P} [26]. The resulting fibration p between the vacuum manifolds R_1 and R_{P} is

$$R_2 \hookrightarrow R_1 \xrightarrow{p} R_{\text{P}}, \quad (24)$$

leading to an interesting relationship between the homotopy groups of different vacuum manifolds

$$\pi_n(R_1, R_2) \cong \pi_n(R_{\text{P}}). \quad (25)$$

Consequently, for $n = 1$ this relationship suggests that the polar phase linear topological defects, namely HQVs and singly quantized vortices, are conserved as linear topological objects in the subsequent second order phase transition. To assess whether the resulting linear objects are composite topological defects, one must calculate the exact sequences of $\pi_1(R_1, R_2)$. Similarly, one can extract information about string-monopole composite defects [27] by setting $n = 2$ in Eq. (25). The resulting topological objects are discussed in Sec. 3.

2.3. Residual symmetries in the presence of orientation energies

The residual symmetries may be broken further by introduction of spatial dependence via confinement (orbital space) or by applied magnetic field (spin space). In this section, we will discuss the consequences of such broken symmetries in specific scenarios.

2.3.1. Polar and PdA phases The presence of various effects, such as liquid-surface interactions, Zeeman splitting, and spin-orbit interaction affect the underlying symmetries. In particular, the presence of anisotropic confinement by nafen breaks the three-dimensional rotational symmetry of the orbital space $SO(3)_{\mathbf{L}}$ in the normal phase.

The consequence in the superfluid phase is that, due to liquid-surface interactions, the presence of anisotropic confinement fixes the direction of one of the orbital vectors ($\hat{\mathbf{m}}$ on polar and PdA phases) in the order parameter. Rotations of the orbital space with respect to perpendicular axes become prohibited, and as a result the orbital symmetry $\mathbb{Z}_{2(\phi+\mathbf{L})}$ in the polar and PdA phases is broken. We note that regions with $-\hat{\mathbf{m}}$ can be converted to regions with $\hat{\mathbf{m}}$ via the identity transformation $(\hat{\mathbf{d}}, \hat{\mathbf{m}}) \rightarrow (-\hat{\mathbf{d}}, -\hat{\mathbf{m}})$ (or $(\hat{\mathbf{d}}, \hat{\mathbf{m}}, \hat{\mathbf{n}}) \rightarrow (-\hat{\mathbf{d}}, -\hat{\mathbf{m}}, -\hat{\mathbf{n}})$ in the PdA phase) and are therefore degenerate. Without loss of generality, we can set $\hat{\mathbf{m}} \parallel \hat{\mathbf{z}}$ everywhere.

On the other hand, the spin-orbit coupling (SOC) energy is proportional to $\propto (\hat{\mathbf{d}} \cdot \hat{\mathbf{m}})^2$, which favors $\hat{\mathbf{d}}$ orientation in the plane perpendicular to the nafen anisotropy axis in the polar and PdA phases. In addition, there is a magnetic energy term proportional to $(\mathbf{B} \cdot \hat{\mathbf{d}})^2$, which orients $\hat{\mathbf{d}} \perp \mathbf{B}$ at sufficiently large magnetic fields (above about 3 mT). For a tilted field $\mathbf{B} \nparallel \hat{\mathbf{m}}$, the combination of the spin-orbit and magnetic energies breaks the $SO(2)_{\mathbf{S}}$ symmetry, resulting in the residual symmetries

$$\tilde{H}_{\text{P}} = SO(2)_{\mathbf{L}} \times \mathbb{Z}_{2(\phi+\mathbf{S})} \times T \times C \times PU_{\pi} \quad (26)$$

and

$$\tilde{H}_{\text{PdA}} = \mathbb{Z}_{2(\phi+\mathbf{S})} \times \mathbb{Z}_{2(T+\mathbf{L})} \times C \times PU_{\pi}. \quad (27)$$

The existence of the symmetry group $\mathbb{Z}_{2(\phi+\mathbf{S})}$ signifies that there are two degenerate minimum energy states which can be obtained via transformation $(\hat{\mathbf{d}}, \phi) \rightarrow (-\hat{\mathbf{d}}, \phi + \pi)$. Such degenerate regions are connected by topological $\hat{\mathbf{d}}$ solitons, which can be terminated in free space by HQVs with π phase winding. We note that similar consideration holds for the spin part of the A phase, where the residual symmetries in the presence of magnetic and spin orbit energies become

$$\tilde{H}_{\text{A}} = U(1)_{\phi+\mathbf{L}} \times \mathbb{Z}_{2(\phi+\mathbf{S})} \times \mathbb{Z}_{2(T+\mathbf{L})} \times C \times PU_{\pi}, \quad (28)$$

which also contains the two degenerate ground states connected by the $\mathbb{Z}_{2(\phi+\mathbf{S})}$ symmetry and supports HQVs.

It is worth noting that the symmetry considerations above concern an ideal confinement without random inhomogeneity. In practical samples, fluctuations of the density of confining strands leads to formation of the Larkin-Imry-Ma (LIM) orbital glass state in the PdA phase. Originally, LIM state was discovered in the A phase confined in the isotropic aerogels [28, 29], where random anisotropy breaks long-range order of the orbital vector $\hat{\mathbf{I}}$ and orientation of $\hat{\mathbf{I}}$ fluctuates over all possible directions in 3D space with a characteristic length scale significantly smaller than the dipolar length ξ_{D} . In the PdA phase under strong anisotropic columnar confinement, $\hat{\mathbf{I}}$ is fixed into the plane perpendicular to the confining strands. There is a clear experimental evidence [30, 31] that also in this case the long-range orientational order of $\hat{\mathbf{I}}$ within this plane is lost, and 2D LIM state is formed. Formation of LIM does not eliminate $\mathbb{Z}_{2(\phi+\mathbf{S})}$ symmetry responsible for the existence of solitons considered in this work, but it does modify the NMR response.

Another way to introduce a discrete \mathbb{Z}_2 symmetry is to confine superfluid ^3He into a narrow slab. Independently of the original superfluid phase, the boundary orients the orbital momentum of the Cooper pairs along the surface normal. Two states connected with \mathbb{Z}_2 symmetry correspond to the orbital momentum oriented towards or away from the wall. The corresponding solitons or domain walls connecting two states were observed both in the B [32] and A [33, 34, 35] phases. At the conditions near the phase transition between A and B phases such walls can proliferate and create a spatially modulated order parameter [32]. In the A phase, reorientation of the orbital momentum can take place independently or in combination with $\hat{\mathbf{d}}$, owing to the spin-orbit coupling. In the latter case the soliton is relatively thick, of the order of the slab thickness, and has been directly visualized by magnetic resonance imaging [35].

2.3.2. PdB phase The orientational energies with different coupling strengths and hierarchy of characteristic length scales reduce the normal phase symmetry group, resulting in reduced degrees of freedom for the order parameter vacuum manifolds after SSB phase transitions. The reduced vacuum manifolds introduce a different set of topological objects than those generated through fibration, discussed in Sec. 2.2.4. For example, in the PdB phase, the orientation energies allow the topological objects described by $\pi_n(R_1, R_2)$ to expand into mesoscopic length scales, forming a nexus [36, 37, 38], discussed in Sec. 3.2. In this section, we will discuss the reduction of the vacuum manifold at mesoscopic length scales.

In ^3He the relevant length scales are the magnetic length ξ_{H} and the dipole length ξ_{D} [3, 39], which characterize the spatial ranges in which the gradient energy dominates over the orientational energy. When the length scale of the spatial variation is larger than these characteristic length scales, the vacuum manifolds are reduced to minimize the orientation energies. The magnetic healing length ξ_{H} is determined by the gradient energy density

$$f_{\nabla} = \frac{1}{2}K_1\partial_i A_{\alpha j}^{\text{PdB}}\partial_i (A_{\alpha j}^{\text{PdB}})^* + \frac{1}{2}K_2\partial_j A_{\alpha i}^{\text{PdB}}\partial_i (A_{\alpha j}^{\text{PdB}})^* + \frac{1}{2}K_3\partial_i A_{\alpha i}^{\text{PdB}}\partial_j (A_{\alpha j}^{\text{PdB}})^*, \quad (29)$$

where $K_1 = K_2 = K_3$ [3]. The magnetic energy density is

$$f_{\text{H}} = -\frac{1}{2}\chi_{\alpha\beta}H_{\alpha}H_{\beta} = \frac{1}{2}\gamma^2 S_a S_b (\chi^{-1})_{ab} - \gamma H_a S_a, \quad (30)$$

where the $\chi_{\alpha\beta}$ is the uniaxial magnetic susceptibility tensor of the PdB phase, H_{α} are magnetic field strengths with $\alpha = 1, 2, 3$, S_a are spin densities with $a = 1, 2, 3$, and γ is the gyromagnetic ratio of ^3He [3]. Using Eqs. (29) and (30) allows writing the magnetic length as

$$\xi_{\text{H}} = \sqrt{\frac{K_1\Delta_{\text{PdB}}^2}{(\chi_{\perp} - \chi_{\parallel})H^2}}, \quad (31)$$

where χ_{\perp} and χ_{\parallel} are transverse and longitude spin magnetic susceptibilities of PdB phase. If a static magnetic field $\mathbf{H}^{(0)}$ with fixed direction is turned on [40], the degenerate space of the PdB order parameter reduces to

$$R_1^{\text{H}} = S_{\mathbf{S}}^1 \times U(1)_{\phi} \quad (32)$$

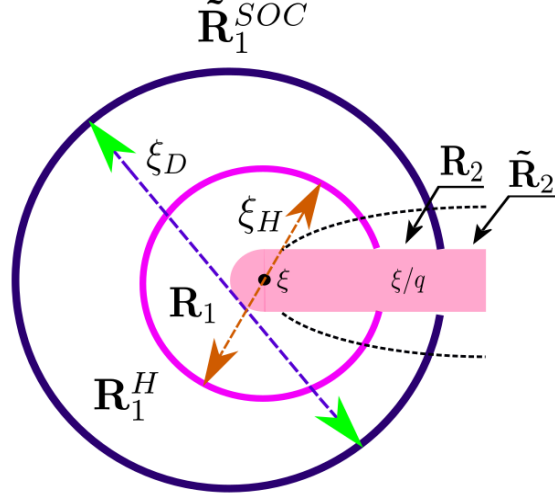


Figure 4. Illustration of vacuum manifolds with length scales $\xi_H < r < \xi_D$ and $r > \xi_D$. The vacuum manifolds of PdB in the vicinity of the second symmetry breaking are R_1 and R_2 in the region with $r < \xi_H$. The hierarchy of length scales extends in the presence of magnetic energy and SOC energy. We have known there is KLS string wall described by $\pi_1(R_1, R_2) \cong \mathbb{Z}$ for $r < \xi_H$. In larger region with length scale $\xi_H < r < \xi_D$, R_1 reduces to $R_1^H = S_S^1 \times U(1)^\Phi$, then spin vector $\hat{\mathbf{d}}$ is perpendicular to static magnetic field $\mathbf{H}^{(0)}$, while the R_2 is unchanged. When the SOC energy is taken into account, R_1^H further reduces to $\tilde{R}_1^{\text{SOC}} = R_S^{\text{SOC}} \times U(1)^\Phi$ and R_2 reduces to $\tilde{R}_2 = \mathbb{Z}_2^{S-\Phi}$.

in the region where length scale of spatial variation is larger than ξ_H . Because the magnetic energy locks the $\hat{\mathbf{d}}$ vector into the plane perpendicular to $\mathbf{H}^{(0)}$, R_2 retains its form inside the region characterized by the length scale ξ_H . It follows that $R_2 = SO(2)_{\mathbf{J}} \times \mathbb{Z}_{2(\phi+\mathbf{S})}$ in the region where $\hat{\mathbf{d}}$ is approximately constant. In Fig. 4, we illustrate the R_1^H and ξ_H in the presence of the KLS wall.

Following the same idea, the dipole length ξ_D is determined by the gradient energy density f_{∇} and the spin-orbit coupling (SOC) energy density

$$f_{\text{SOC}} = \frac{3}{5}g_D \left((A_{ii}^{\text{PdB}})^* A_{jj} + (A_{ij}^{\text{PdB}})^* A_{ji} - \frac{2}{3} (A_{ij}^{\text{PdB}})^* A_{ij} \right), \quad (33)$$

where g_D is the strength of the spin orbital coupling. Then we have

$$\xi_D = \sqrt{\frac{5K_1}{6g_D}}. \quad (34)$$

When the SOC is taken into account, the vacuum manifolds are further reduced from R_1^H and R_2 . In general, the requirement of minimizing the SOC energy in the region with $r > \xi_D$ fixes the relative directions between spin and orbital vectors, resulting in the broken relative spin-orbit symmetry [3]. Thus R_1^H reduces to

$$\tilde{R}_1^{\text{SOC}} = R_S^{\text{SOC}} \times U(1)_\phi \quad (35)$$

in the region with $r > \xi_D$, where R_S^{SOC} is the reduced vacuum manifold of the spin degree of freedom. Generally speaking, R_S^{SOC} has a complicated form, which may be

simplified by using the following parametrization

$$\hat{\mathbf{d}} = \hat{\mathbf{x}} \cos \theta - \hat{\mathbf{z}} \sin \theta, \quad \hat{\mathbf{e}}^1 = -\hat{\mathbf{x}} \sin \theta - \hat{\mathbf{z}} \cos \theta, \quad \hat{\mathbf{e}}^2 = \hat{\mathbf{y}}, \quad \mathbf{H}^{(0)} = H\hat{\mathbf{y}}, \quad (36)$$

where θ is the angle between $\hat{\mathbf{d}}$ and local orbital-coordinate frame [40]. In this case, we find

$$R_{\mathbf{S}}^{\text{SOC}} = \{\theta_0, \pi - \theta_0, -\theta_0, \pi + \theta_0\}, \quad (37)$$

where $\theta_0 = \arcsin(q/(1 - |q|))$. In the region where $\hat{\mathbf{d}}$ is approximately constant, the SOC energy fixes the relative rotation of $SO(2)_{\mathbf{J}}$, reducing R_2 to

$$\tilde{R}_2 = \mathbb{Z}_{2(\phi+\mathbf{s})} \quad (38)$$

in the region $r > \xi_{\text{D}}$.

The groups R_1^{H} , \tilde{R}_1^{SOC} , and \tilde{R}_2 are illustrated in Fig. 4. The relative homotopy groups may again be utilized to investigate topological objects in the presence of multiple characteristic length scales [41]. This system with multiple length scales belongs to type (i) of the classifications in Ref. [37]. Other recent examples of this class include solitons terminated by HQVs in spinor Bose condensates with quadratic Zeeman energy [42, 43]. Both of these systems can be described by the first relative homotopy group π_1 .

3. Composite topological objects

In this section we will discuss various composite objects that are connected by solitons in different superfluid phases of ${}^3\text{He}$.

3.1. Relative homotopy groups – from polar to polar-distorted phases

In experimentally reachable magnetic field $\mathbf{H}^{(0)}$ the magnetic healing length is much larger than the coherence length, $\xi_{\text{H}} \gg \xi_0$. The symmetry group G' and the symmetry breaking pattern described by Eq. (20) are valid in the region $\xi_0 \ll r \leq \xi_{\text{H}}$. In Sec. 2.2.4, we have seen that the polar-phase topological objects survive a second symmetry-breaking transition into either PdA or PdB phases. In this section, we will study how these objects change in the transition to the PdA and PdB by analyzing the relative homotopy groups $\pi_n(R_1, R_2)$. The structures of the relative homotopy groups $\pi_n(R_1, R_2)$ can be extracted from their short exact sequences (SES). The SESs are calculated by splitting the long exact sequences of $\pi_n(R_1, R_2)$. In this section we use the results calculated in Appendix A.1 and Appendix A.2.

The SES of $\pi_1(R_1^{\text{PdA}}, R_2^{\text{PdA}})$ is

$$0 \longrightarrow \mathbb{Z}_{\phi} \longrightarrow \pi_1(R_1^{\text{PdA}}, R_2^{\text{PdA}}) \xrightarrow{\partial^*} 0 \longrightarrow 0 \quad (39)$$

and SES of $\pi_2(R_1^{\text{PdA}}, R_2^{\text{PdA}})$ is

$$0 \longrightarrow \mathbb{Z}_{\mathbf{S}} \longrightarrow \pi_2(R_1^{\text{PdA}}, R_2^{\text{PdA}}) \xrightarrow{\partial^*} 0 \longrightarrow 0, \quad (40)$$

where the vacuum manifolds R_1^{PdA} and R_2^{PdA} are given by Eqs. (14) and (15). From the SESs of $\pi_{1(2)}(R_1^{\text{PdA}}, R_2^{\text{PdA}})$ in Eqs. (39) and (40), we find that the boundary

homomorphisms ∂^* are trivial both for $\pi_1(R_1, R_2)$ and $\pi_2(R_1, R_2)$ in the PdA phase. In other words, linear and point-like defects (HQVs and \mathbf{d} -monopoles, respectively), which PdA phase inherits from polar phase, are simple (i.e. not composite) topological objects. Due to similar spin structure, the HQVs and \mathbf{d} -monopoles are similar in both phases [36].

In contrast, the symmetry breaking pattern resulting in the PdB phase yields non-trivial results. The SESs of $\pi_1(R_1, R_2)$ and $\pi_2(R_1, R_2)$ in the PdB phase have non-trivial boundary homomorphisms. Specifically, we have

$$0 \longrightarrow \mathbb{Z}_\phi \longrightarrow \pi_1(R_1^{\text{PdB}}, R_2^{\text{PdB}}) \xrightarrow{\partial^*} \mathbb{Z}_{2(\phi+\mathbf{s})} \longrightarrow 0 \quad (41)$$

and

$$0 \longrightarrow 0 \longrightarrow \pi_2(R_1^{\text{PdB}}, R_2^{\text{PdB}}) \xrightarrow{\partial^*} 2\mathbb{Z}_{\mathbf{J}} \longrightarrow 0, \quad (42)$$

where $R_1^{\text{PdB}}, R_2^{\text{PdB}}$ are given by Eqs. (18) and (19). The homotopy group $\mathbb{Z}_{2(\phi+\mathbf{s})} = \pi_0(R_2^{\text{PdB}})$ gives rise to the Kibble-Lazarides-Shafi (KLS) domain wall [44, 45] owing to the disconnected vacuum manifold R_2^{PdB} discussed in Sec. 2.2.3. The homotopy group $2\mathbb{Z}_{\mathbf{J}} \subset \pi_1(R_2^{\text{PdB}})$ describes spin vortices with an even winding number [36].

Non-trivial boundary homomorphisms ∂^* in Eqs. (41) and (42) describe how low dimensional objects, e.g. KLS walls and spin vortices, connect to objects with higher dimensionality. Here we have considered HQVs and \mathbf{d} -monopoles, inherited from the polar phase. We refer to the resulting composite objects consisting of D -dimensional and $(D+1)$ -dimensional objects, as string-walls and string-monopoles, respectively, based on the rank of their relative homotopy groups [36].

3.2. Vortex-bound solitons in the PdB phase and the nexus object

We now know that the PdB phase supports several composite topological objects with different dimensions, contained in length scales smaller than ξ_{H} . However, typical NMR experiments probe superfluid properties at length scales larger than ξ_{H} , which poses a question: what happens to composite objects at length scales approaching ξ_{H} ? This question is both theoretically interesting and relevant for understanding experimental observations, as composite objects with characteristic length scales ξ_0 or $\xi_0/|q|$ cannot be observed directly with NMR methods.

Composite defects, such as walls bounded by strings studied in Ref. [40], can be identified from the NMR signature of the related spin solitons. HQVs can therefore be considered as one dimensional (1D) nexuses connecting defects with different characteristic sizes [37, 38]. In this section, we will discuss the relative homotopy groups for the reduced vacuum manifolds analyzed in Sec. 2.3.2. We will see how HQVs and KLS walls with characteristic length scales ξ and $\xi/|q|$, respectively, connect to spin solitons with much larger characteristic length scale, set by the dipole length ξ_{D} . In this problem the length scales are well separated, $\xi_{\text{D}} \gg \xi_0/|q| \gg \xi_0$ [37]. For technical details, we refer the reader to Appendix A.3.

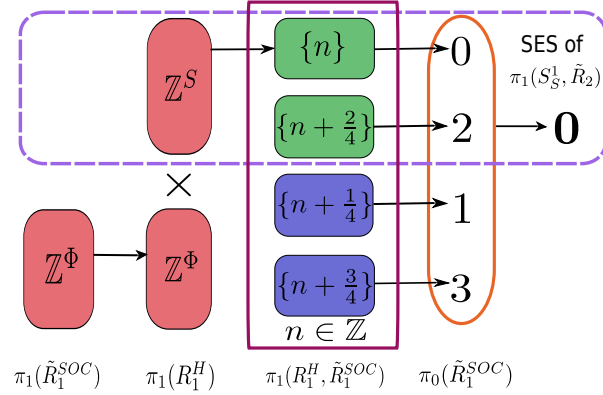


Figure 5. Illustrations of LES of $\pi_1(R_1^H, \tilde{R}_1^{\text{SOC}})$ and SES $\pi_1(S_{\mathbf{S}}^1, \tilde{R}_2)$. This mapping diagram demonstrates that the linear objects of $\pi_1(R_1^H, \tilde{R}_1^{\text{SOC}})$ are spin solitons. This is because the mapping between $\pi_1(\tilde{R}_1^{\text{SOC}})$ and $\pi_1(R_1^H)$ is projection, the image of homomorphism $i^* : \pi_1(\tilde{R}_1^{\text{SOC}}) \rightarrow \pi_1(R_1^H) = \mathbb{Z}_\phi$ i.e., topological invariant of all phase vortices. As a result, the trivial linear objects of $\pi_1(R_1^H, \tilde{R}_1^{\text{SOC}})$ are all phase vortices because of $\text{Im}[i^*] \cong \ker[j^*]$. We found three kinds of spin solitons because $\ker[k^*] \cong \text{Im}[\partial^*] = \mathbb{Z}_4$. Moreover, this illustration shows that the subgroup $G = \{[n], [n + 2/4]\}$ of $\pi_1(R_1^H, \tilde{R}_1^{\text{SOC}})$ is extension of $\mathbb{Z}_{\mathbf{S}}$ by $\pi_0(\tilde{R}_2^{\text{SOC}}) = \mathbb{Z}_2$ and then isomorphic to M . Marked by the dashed line is the corresponding SES of G_{sub} . As a result, HQV is a 1D nexus between the spin soliton of coset $[2/4]$ and the KLS wall in the PdB phase [37].

3.2.1. Walls bounded by strings In the region $\xi_{\text{H}} < r < \xi_{\text{D}}$, the SES of $\pi(R_1^H, R_2)$ is

$$0 \longrightarrow \mathbb{Z}_\phi \longrightarrow \pi_1(R_1^H, R_2) \xrightarrow{\partial^*} \mathbb{Z}_{2(\phi+\mathbf{s})} \longrightarrow 0 . \quad (43)$$

Eq. (43) determines how linear defects with a characteristic length scale $\xi_{\text{H}} < r < \xi_{\text{D}}$ connect with a possible domain wall. Eq. (43) suggests

$$\pi_1(R_1^H, R_2) \cong \tilde{\mathbb{Z}}, \quad (44)$$

which is isomorphic to $\pi_1(R_1, R_2)$ within ξ_{H} . In other words the KLS wall, determined by two length scales ξ and ξ/q , extends into the region $\xi_{\text{H}} \leq r \leq \xi_{\text{D}}$. However, Eq. (43) only contains the phase factor ϕ . In particular, all information about the spin degrees of freedom is lost as they are trivial elements of $\pi_1(R_1^H, R_2)$. To restore the spin part of the KLS wall, we recall that the domain wall connects regions with $(\mathbf{d}, \mathbf{e}^1, q, \phi)$ and $(-\mathbf{d}, -\mathbf{e}^1, -q, \pi + \phi)$ [46]. However, Eq. (44) only catches the phase degree of freedom, i.e. phase vortices. Similarly, the spin degree of freedom can be described by the group

$$M \equiv \{n_{\mathbf{S}}/2 | n_{\mathbf{S}} \in \mathbb{Z}\}, \quad (45)$$

such that $M/\pi_1(S_{\mathbf{S}}^1) \cong \mathbb{Z}_2 = \{[0], [1/2]\}$, where $\pi_1(S_{\mathbf{S}}^1) \subset \pi_1(R_1^H)$ represents free spin vortices. The cosets $[0]$ and $[1/2]$ correspond to the absence or presence of the KLS string wall in the region $\xi_{\text{H}} < r \leq \xi_{\text{D}}$, respectively. Coset $[0] \cong 2\mathbb{Z}$ contains all integer spin vortices, while the Coset $[1/2] \cong \{n + 1/2 | n \in \mathbb{Z}\}$ contains all half-integer spin vortices, including the HQV. These properties are equivalent to SES

$$0 \longrightarrow \mathbb{Z}_{\mathbf{S}} \longrightarrow M \xrightarrow{\partial^*} \mathbb{Z}_{2(\phi+\mathbf{s})} \longrightarrow 0 . \quad (46)$$

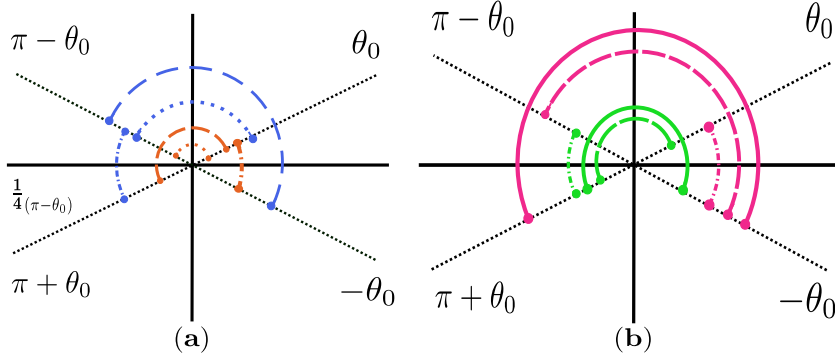


Figure 6. Illustration of spin solitons corresponding to $\pi_1(S_{\mathbf{S}}^1, R_{\mathbf{S}}^{\text{SOC}})$ [37]. The black fine dotted lines represent the four elements of $R_{\mathbf{S}}^{\text{SOC}}$ i.e., $\pm\theta_0$ and $\pi \pm \theta_0$. The colored dashed, sparse dotted, dash-dotted and solid lines correspond to π -soliton ($|\Delta\theta| = \pi$), soliton ($|\Delta\theta| = \pi - 2\theta_0$), KLS-soliton ($|\Delta\theta| = 2\theta_0$) and big-soliton ($|\Delta\theta| = \pi + 2\theta_0$), respectively. (a) Spin solitons with topological invariants $1/4$, $2/4$ and $3/4$ originating at θ_0 (orange) and $\pi - \theta_0$ (blue), respectively. (b) Spin solitons with topological invariants $1/4$, $2/4$ and $3/4$ originating at $-\theta_0$ (pink) and $\pi + \theta_0$ (green), respectively.

3.2.2. Spin solitons For $r > \xi_D$, R_1^H reduces to $\tilde{R}_1^{\text{SOC}} = R_{\mathbf{S}}^{\text{SOC}} \times U(1)_\phi$. The resulting linear objects are classified by the homotopy group $\pi_1(R_1^H, \tilde{R}_1^{\text{SOC}})$ which has the SES

$$0 \longrightarrow \mathbb{Z}_{\mathbf{S}} \longrightarrow \pi_1(R_1^H, \tilde{R}_1^{\text{SOC}}) \xrightarrow{\partial^*} \mathbb{Z}_4 \longrightarrow 0. \quad (47)$$

It follows that

$$\pi_1(R_1^H, \tilde{R}_1^{\text{SOC}}) = \{n_{\mathbf{S}}/4 | n_{\mathbf{S}} \in \mathbb{Z}\} \cong \mathbb{Z}, \quad (48)$$

and

$$\pi_1(R_1^H, \tilde{R}_1^{\text{SOC}})/\mathbb{Z}_{\mathbf{S}} \cong \mathbb{Z}_4. \quad (49)$$

Because Eq. (47) is determined by $\mathbb{Z}_{\mathbf{S}} = \pi_1(S_{\mathbf{S}}^1)$ and $\mathbb{Z}_4 = \pi_0(R_{\mathbf{S}}^{\text{SOC}})$ (see details in Appendix A.3), we have

$$\pi_1(R_1^H, \tilde{R}_1^{\text{SOC}}) = \pi_1(S_{\mathbf{S}}^1, R_{\mathbf{S}}^{\text{SOC}}). \quad (50)$$

Eq.(50) signifies that the linear objects classified by $\pi_1(R_1^H, \tilde{R}_1^{\text{SOC}})$ only involve the spin degree of freedom, i.e. they are spin solitons and spin vortices [47, 36]. The four cosets of $\pi_1(S_{\mathbf{S}}^1, R_{\mathbf{S}}^{\text{SOC}})$ are

$$[0] = \{n_{\mathbf{S}}\}, \quad \left[\frac{1}{4}\right] = \left\{n_{\mathbf{S}} + \frac{1}{4}\right\}, \quad \left[\frac{2}{4}\right] = \left\{n_{\mathbf{S}} + \frac{2}{4}\right\}, \quad \text{and} \quad \left[\frac{3}{4}\right] = \left\{n_{\mathbf{S}} + \frac{3}{4}\right\}. \quad (51)$$

These cosets give the topological invariants of the four types of linear objects corresponding to spin vortices and three types of spin solitons. Fig. 6 shows the representatives of spin solitons of $\pi_1(S_{\mathbf{S}}^1, R_{\mathbf{S}}^{\text{SOC}})$. Following the terminology in Ref. [40], they are big-soliton ($|\Delta\theta| = \pi + 2\theta_0$), soliton ($|\Delta\theta| = \pi - 2\theta_0$), KLS-soliton ($|\Delta\theta| = 2\theta_0$), and π -soliton ($|\Delta\theta| = \pi$). Spin vortices, i.e. the coset $[0]$, are not discussed further as they are outside the scope of this review.

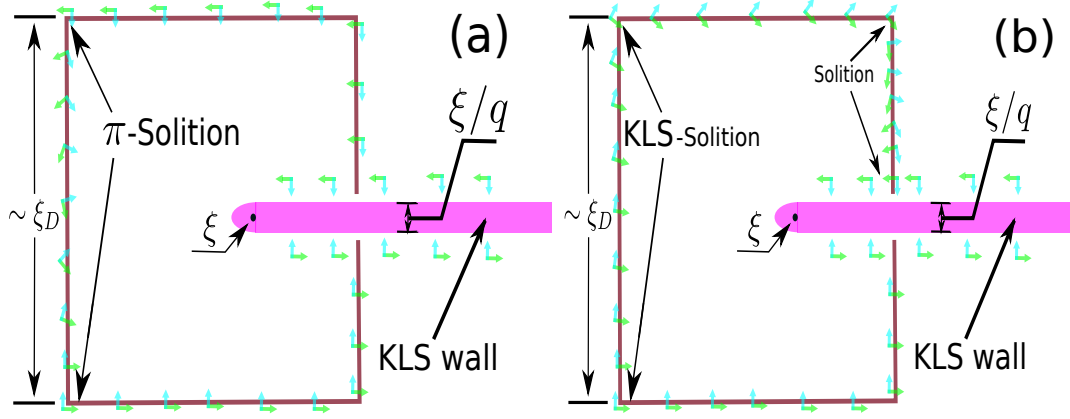


Figure 7. Illustrations of two different spin configurations of 1D nexus object, which consists of spin solitons, HQV and KLS domain wall. The green and cyan arrows represent the $\hat{\mathbf{d}}$ and $\hat{\mathbf{e}}$ vectors respectively. (a) Configuration of inseparable spin soliton. In this configuration, the topological invariant of spin soliton is $1/2$, which corresponds to π -soliton. (b) In this configuration there are two spin solitons with topological invariant $1/4$ when the group $\pi_1(S_S^1, \tilde{R}_2)$ is implemented in alternative way. Following the requirement of continuity of order parameter, these two spin solitons are KLS-soliton ($\Delta\theta = 2\theta_0$) and soliton ($\Delta\theta = \pi - 2\theta_0$).

A significant property of $\pi_1(S_S^1, R_S^{\text{SOC}})$ is that it has a subgroup $G_{\text{sub}} \equiv \{[0], [2/4]\}$ such that $G_{\text{sub}}/\mathbb{Z}_S \cong \mathbb{Z}_2$. It follows that the SES of G_{sub} is given by Eq. (47) as

$$0 \longrightarrow \mathbb{Z}_S \longrightarrow G_{\text{sub}} \xrightarrow{\partial^*} \mathbb{Z}_2 \longrightarrow 0. \quad (52)$$

The mapping diagram of Eq. (52) is shown as the dashed panel in Fig. 5. Comparing Eqs. (46) and (52) leads to

$$G_{\text{sub}} = \pi_1(S_S^1, \tilde{R}_2) \cong \hat{\mathbb{Z}} = M, \quad (53)$$

where $\hat{\mathbb{Z}} \equiv \{n_S/2 | n_S \in \mathbb{Z}\}$.

Eq. (53) suggests that one can continuously transform spin solitons, classified by the $[2/4]$ coset of $\pi_1(S_S^1, \tilde{R}_2)$, to half spin vortices of M . In other words, the KLS wall smoothly connects to the $[2/4]$ spin soliton via a HQV. Similarly to a 2D nexus connecting the string monopole and the vortex skyrmion [36, 38], the HQV is a 1D nexus connecting the KLS wall and the $[2/4]$ spin soliton [37]. The composite object formed by the $[2/4]$ spin soliton and the KLS wall is called the 1D nexus object.

3.2.3. The 1D nexus object Because $\pi_1(S_S^1, R_S^{\text{SOC}})/\mathbb{Z}^S \cong \mathbb{Z}_4$, we have $[2/4] = [1/4] + [1/4]$. Thus $\pi_1(S_S^1, \tilde{R}_2)$ could also be represented as $\{[0], [1/4] + [1/4]\}$ besides $\pi_1(S_S^1, \tilde{R}_2) \cong \{[0], [2/4]\}$. This means there are two kinds of spin soliton configurations connecting with KLS domain wall via HQV for a given element of $\pi_1(S_S^1, \tilde{R}_2)$. When the topological invariant is $2/4$, the spin soliton is spatially inseparable π -soliton see Figs. 7(a).

When the topological invariant is $1/4 + 1/4$, the spin soliton is combination of two spatially separable spin solitons with topological invariant $1/4$. These two spatially

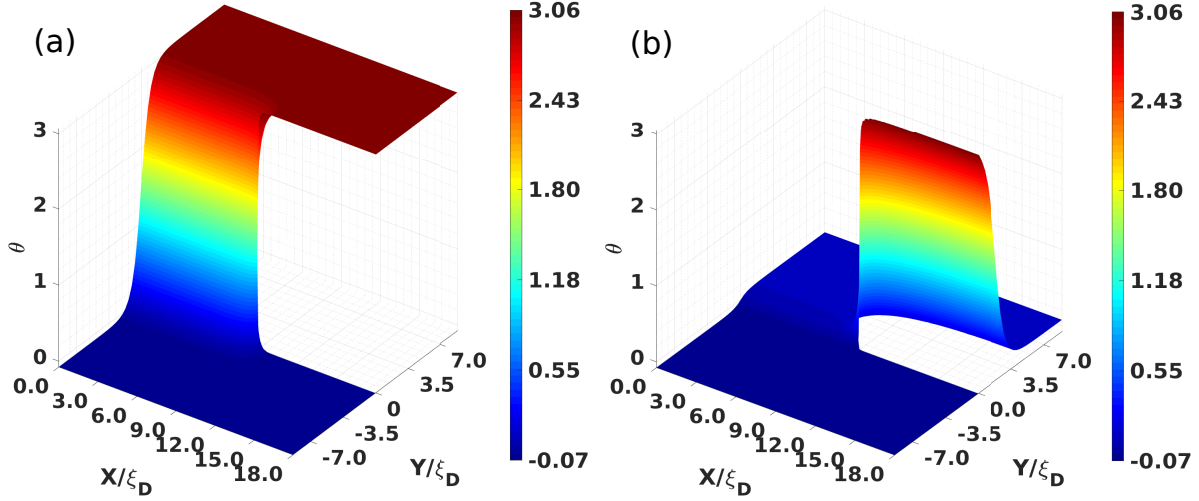


Figure 8. Numerically calculated equilibrium configurations of inseparable and separable spin solitons in one-half unit cell with $|q| = 0.18$ and $D = 18\xi_D$. (a) Inseparable configuration with π -soliton, corresponding to the sketch in Fig. 7a. (b) Separable configuration with combination of KLS-soliton and soliton, corresponding to the sketch in Fig. 7b.

separated spin solitons are the KLS soliton ($|\Delta\theta| = 2\theta_0$) and soliton ($|\Delta\theta| = \pi - 2\theta_0$). As illustrated in Fig. 7(b), the 1D nexus object contains two spin solitons. As we will see in Sec. 4, the free energies and spin textures of the two cases are quite different [37], resulting in distinguishable dynamic spin response properties and NMR frequency shifts. Those are calculated based on numerically found minimum-energy configurations as illustrated in Fig. 8.

3.3. Vortex-bound solitons in the polar phase

In the polar phase, the solitons are bound by HQVs. The existence of HQVs was predicted decades ago in $^3\text{He-A}$ [48] and observed recently in the polar phase of ^3He [39]. Previously, HQVs have been observed in grain boundaries of d -wave cuprate superconductors [49], in superconductor rings [50], and in Bose condensates [51, 52]. In p -wave superfluids such as ^3He , HQVs provide access to vortex-core-bound fermion states, which have been predicted to harbor non-Abelian anyons in 2D $p_x + ip_y$ superconductors and superfluids [53, 54, 55].

In the polar phase the presence of magnetic field larger than the dipole field, $H > 3\text{mT}$, fixes the spin anisotropy vector $\hat{\mathbf{d}} = \hat{\mathbf{i}} \cos\theta(\mathbf{r}) + \hat{\mathbf{j}} \sin\theta(\mathbf{r})$ in Eq. (9) via the spin-orbit interaction $F_{\text{so}} \propto (\hat{\mathbf{d}} \cdot \hat{\mathbf{m}})^2$ to the plane perpendicular to \mathbf{H} . Vectors $\hat{\mathbf{i}}$ and $\hat{\mathbf{j}}$ are mutually orthogonal unit vectors in the plane normal to \mathbf{H} . The orbital anisotropy vector $\hat{\mathbf{m}}$ is pinned parallel to nafen strands, $\hat{\mathbf{m}} \parallel \hat{\mathbf{z}}$. The combined effect of the confinement and magnetic field affects the distribution of the $\hat{\mathbf{d}}$ vector such that θ is governed by the Sine-Gordon equation

$$\nabla^2\theta = \frac{1}{2\xi_D^2} \sin^2\mu \sin 2\theta. \quad (54)$$

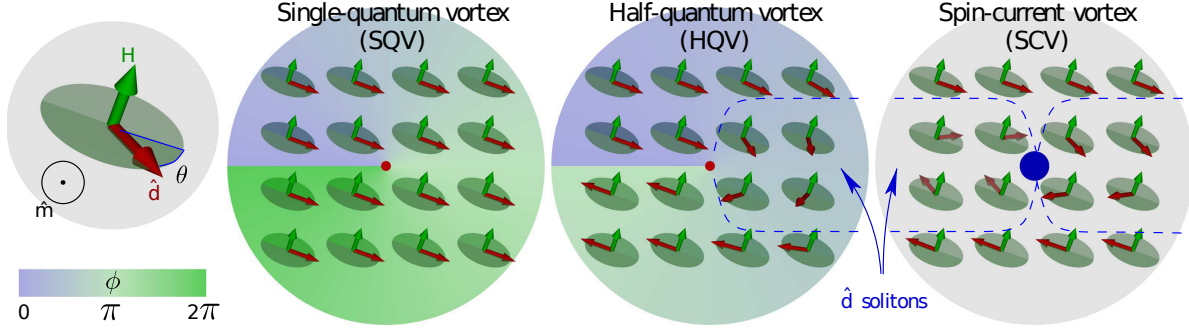


Figure 9. Vortex types in the polar phase. The phase of the order parameter ϕ is shown as the background color. The spin anisotropy vector $\hat{\mathbf{d}}$ is locked to the plane (green disks) perpendicular to the magnetic field \mathbf{H} by magnetic energy. In this plane, the vector $\hat{\mathbf{d}}$ rotates by π around the HQV core and by 2π around the spin vortex core. In a tilted magnetic field ($\mathbf{H} \nparallel \hat{\mathbf{m}}$) the reorientation of the $\hat{\mathbf{d}}$ vector is concentrated in one or two solitons (illustrated with dashed lines) with π winding, terminating at the HQV or at the spin vortex core, respectively. The nafen strands, oriented along $\hat{\mathbf{m}}$, and the vortex lines are orthogonal to the figure. The phase vortex and the HQV have hard cores (red discs) of the size of coherence length $\xi \sim 40$ nm, while the spin vortex has a soft core (blue disc) of much larger dipolar size $\xi_D \sim 10$ μm .

Here $\xi_D \sim 10$ μm is the dipole length and μ is the angle of the magnetic field with respect to $\hat{\mathbf{z}}$.

The polar phase order parameter supports three different vortex types illustrated in Fig. 9 – the singly quantized phase vortices, the spin-current vortices (SCV), and the HQVs. Reorientation of $\hat{\mathbf{d}}$ outside of SCV and HQV cores is governed by solitonic solutions of Eq. (54). In tilted $\mathbf{H} \nparallel \hat{\mathbf{z}}$ field the SCV terminates two π -solitons, while the HQV terminates just one. Additionally, solitons may be terminated at the sample boundary. The soliton width is fixed by the characteristic length scale $\sim \xi_D / \sin \mu$. For $\mathbf{H} \parallel \hat{\mathbf{z}}$ or at zero magnetic field, all states with $\hat{\mathbf{d}} \perp \hat{\mathbf{m}}$ are degenerate, and solitons are not created.

3.4. Composite spin-mass vortex with soliton tail in ${}^3\text{He-B}$

Spin-mass vortex – a composite defect in superfluid ${}^3\text{He-B}$ [56, 57]. Its existence may be seen from the B-phase order parameter in Eq. (2). This order parameter supports different topological defects, see Fig. 10. In rotation the most usual defect is a mass-current vortex, a conventional quantized vortex line. Around it the phase ϕ winds by 2π , which results in a supercurrent proportional to $\nabla\phi$ around its singular core. Within the core the amplitude of the order parameter $|A_{\alpha j}|$ is depleted from its equilibrium value Δ_B . A second defect is a disclination in the $R_{\alpha j}$ field. It also has a singular core which is encircled by a spin current. On moving once around the core $\hat{\mathbf{n}}$ reverses its direction twice: First by smooth rotation while the angle θ remains at the equilibrium value $\theta_D \approx 104^\circ$, which minimizes the spin-orbit interaction energy. Later by increasing θ to 180° , where both directions of $\hat{\mathbf{n}}$ are equivalent, and then decreasing back to θ_D .

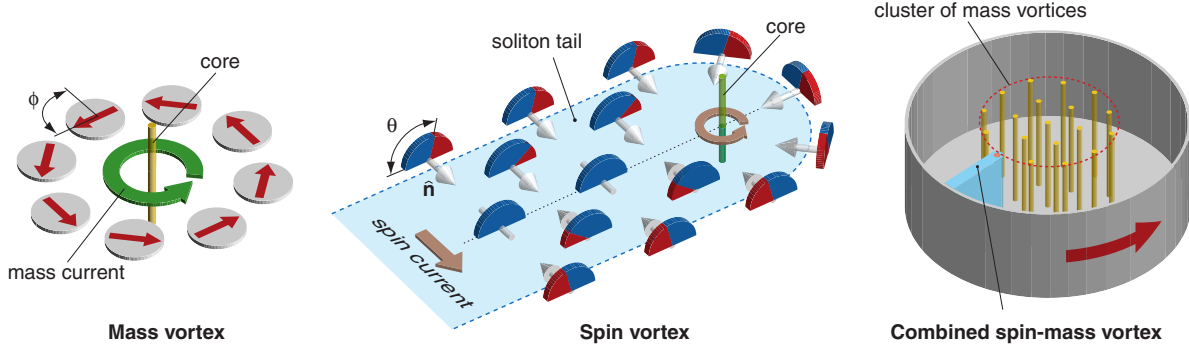


Figure 10. Structure of the spin-mass vortex (SMV) in ${}^3\text{He-B}$. *(Left)* Mass vortex traps winding of phase ϕ around a hard core. *(Center)* Disclination in the orbital rotation field takes form of a soliton tail terminated by a spin vortex with a hard core. *(Right)* When cores of mass and spin vortices merge, a stable configuration of SMV in rotating container is possible.

The second leg in the direction reversal does not minimize the spin-orbit interaction and hence it becomes confined in space within a planar structure, a soliton sheet, which terminates on the linear singular core or on the wall of the container. This structure becomes possible through the existence of two different energy (and length) scales: The superfluid condensation energy defines the scale of the coherence length $\xi \sim 10\text{--}100\text{ nm}$, which is roughly the radius of the singular core. The much weaker spin-orbit interaction defines the scale of the dipolar healing length $\xi_D \sim 10\ \mu\text{m}$, which is approximately the width of the soliton sheet. The detailed topological analysis of the B-phase soliton structures can be found in Ref. [5], where experimentally realized configurations correspond to $(- + 1)$ or $(+ - 1)$ classes in terms of that work.

The spin vortex by itself is an unstable structure: The surface tension of the soliton leads to its annihilation and disappearance. Another composite defect – the combined spin-mass vortex (SMV) – can be stabilized in the rotating container. It has both phase ϕ winding and a $R_{\alpha j}$ disclination trapped on the same core. If the number of mass-current vortex lines in the container is less than that in the equilibrium state in rotation, then the existing lines are confined to a cluster in the center of the container by the Magnus force from the uncompensated normal-superfluid counterflow. Due to the trapped mass current the SMV also experiences the Magnus force which pulls it towards the vortex cluster. This force is opposed by the surface tension of the soliton and as a result its equilibrium position is slightly outside the cluster of mass vortices. The soliton tail of the SMV has a characteristic NMR absorption response which allows its identification.

Another possible stable configuration is the soliton sheet bounded by two SMVs and embedded within the vortex cluster. The size of such pair is set by competition of the surface tension of the soliton sheet, which tries to pull vortices together and repulsion of two mass vortices of the same circulation. The equilibrium size is estimated to be about $6\xi_D$ and it is too small to identify contribution of a single pair in the NMR

spectrum.

4. Spin dynamics and NMR

NMR techniques are used as a non-invasive way to probe properties of different superfluid phases of ^3He . NMR methods are particularly useful for extracting information about the spin-orbit coupling (SOC). This is because the long range coherence in superfluid states enhances the SOC energy [58, 59]. In the superfluid state the observable NMR resonance frequency is often shifted from the Larmor value since the precessing spin experiences an additional torque from SOC. The topological solitons form potential wells for bound spin-wave state, which result in satellite peaks with characteristic frequency shifts. Since the characteristic time scale of SOC is much longer than the microscopic time scales of superfluid, i.e., $\hbar\Delta^{-1}$, the microscopic processes remain in equilibrium under weak magnetic perturbation. In other words, the NMR response is the hydrodynamic response of the spin densities δS_a and spin vectors [3, 60].

Under weak magnetic perturbation $\delta H_a \equiv \delta \mathbf{H}$ along y -axis, the linear response of spin density is

$$\delta S_+(\mathbf{r}, t) = \int d\sigma' \int dt' \frac{\delta S_+}{\delta H_a}(\mathbf{r}, t, \mathbf{r}', t') \delta H_a(\mathbf{r}', t') + O(\delta H_a^2), \quad (55)$$

where $\delta S_+ = [\delta S_1 + i\delta S_3]/\sqrt{2}$ is transverse spin density and $a = 1, 2, 3$ are spatial coordinate indexes. To calculate the response function and its poles, we use method based on hydrodynamic equations [60]. In the limit of hydrodynamics, the system of dynamic equations of spin densities S_α and spin vectors are a system of Liouville equations

$$\frac{\partial S_\alpha}{\partial t} = \{F_{hy}, S_\alpha\}, \quad \frac{\partial V_\alpha^a}{\partial t} = \{F_{hy}, V_\alpha^a\}, \quad (56)$$

where V_α^a denote the three spin vectors of order parameter. These equations are known as Leggett equations [3]. The hydrodynamic free energy of a superfluid dominated by the SOC energy is

$$F_{hy} = \int_\Sigma (f_H + f_{\text{soc}} + f_{\text{grad}}) d\Sigma. \quad (57)$$

Eq. (56) can be rewritten as

$$\frac{\partial S_\alpha}{\partial t} = \int_\Sigma d^3r' \frac{\delta F_{hy}}{\delta S_\beta} (r') \{S_\beta(r'), S_\alpha(r)\} + \int_\Sigma d^3r' \frac{\delta F_{hy}}{\delta V_\beta^a} (r') \{V_\beta^a(r'), S_\alpha(r)\} \quad (58)$$

and

$$\frac{\partial V_\alpha^a}{\partial t} = \int_\Sigma d^3r' \frac{\delta F_{hy}}{\delta S_\beta} (r') \{S_\beta(r'), V_\alpha^a(r)\}, \quad (59)$$

where $\alpha, \beta = 1, 2, 3$ are indexes of spatial components of hydrodynamic variables. The Poisson brackets between S_α and V_α^a are [61]

$$\begin{aligned} \{S_\alpha(r_1), S_\beta(r_2)\} &= \epsilon_{\alpha\beta\gamma} S_\gamma \delta(r_1 - r_2) \\ \{S_\alpha(r_1), V_\beta^a(r_2)\} &= \epsilon_{\alpha\beta\gamma} V_\gamma^a \delta(r_1 - r_2), \end{aligned} \quad (60)$$

where r_1 and r_2 are the spatial coordinates and $\epsilon_{\alpha\beta\gamma}$ is the Levi-Civita symbol.

4.1. Satellite shifts induced by spin solitons in the PdB phase

After plugging Eq. (60) into Eqs. (58) and (59), the coupled first order dynamic equations for spin densities S_α and V_α^a for PdB phase are given as

$$\frac{\partial S_\alpha}{\partial t} = \gamma H_\beta \epsilon_{\alpha\beta\gamma} S_\gamma - \frac{6}{5} g_D V_j^d V_\gamma^b \epsilon_{\alpha\beta\gamma} Q_{\beta j}^{bd} + (\partial_i \partial_j V_\beta^b) V_\gamma^a \epsilon_{\alpha\beta\gamma} K_{ij}^{ba}, \quad (61)$$

$$\frac{\partial V_\alpha^a}{\partial t} = \gamma H_\beta \epsilon_{\alpha\beta\gamma} V_\gamma^a - \delta \gamma^2 \chi_\perp^{-1} S_\eta V_\eta^3 V_\beta^3 \epsilon_{\alpha\beta\gamma} V_\gamma^a - \gamma^2 \chi_\perp^{-1} S_\beta \epsilon_{\alpha\beta\gamma} V_\gamma^a, \quad (62)$$

where $\delta = (\chi_\perp - \chi_\parallel) / \chi_\parallel$ in which χ_\perp and χ_\parallel are the transverse magnetic susceptibility and the longitude magnetic susceptibility of PdB phase respectively.

$$\begin{aligned} K_{ij}^{ba} &= K_1 \delta_{ij} X_m^b X_m^a + K_2 X_j^a X_i^b + K_3 X_j^b X_i^a, \\ Q_{\beta j}^{bd} &= X_\beta^b X_j^d + X_\beta^d X_j^b \end{aligned} \quad (63)$$

with $X_i^1 = \Delta_{\perp 1} \hat{x}_i$, $X_i^2 = \Delta_{\perp 2} \hat{y}_i$, $X_i^3 = \Delta_{\parallel} \hat{z}_i$. Starting from the first order equations of spin densities and degenerate parameters in Eq. (61) and Eq. (62), we can further derive the second order spin dynamic response equations of δS_α under weak magnetic drive δH_α by plugging

$$\begin{aligned} H_\alpha &= H_\alpha^{(0)} + \delta H_\alpha(t) \\ S_\alpha &= S_\alpha^{(0)} + \delta S_\alpha(\mathbf{r}, t) \\ V_\alpha^a &= V_\alpha^{a(0)} + \delta V_\alpha^a(\mathbf{r}, t) \end{aligned} \quad (64)$$

into Eqs. (61) and (62). Here the $S_\alpha^{(0)}$ and $V_\alpha^{a(0)}$ are the equilibrium spin densities and equilibrium degenerate parameters respectively. While the $\delta S_\alpha(\mathbf{r}, t)$ and $\delta V_\alpha^a(\mathbf{r}, t)$ are the dynamic parts of the perturbed spin densities and degenerate parameters. The $H_\alpha^{(0)}$ is the static magnetic field and $\delta H_\alpha(t) = |\delta \mathbf{H}| \hat{x} e^{-i\omega t}$ is the homogeneous RF continuous-wave drive. The derived spin dynamic response equations are

$$\begin{aligned} i\omega \delta S_\alpha(\omega) &= \gamma \epsilon_{\alpha\beta\gamma} H_\beta^{(0)} \delta S_\gamma(\omega) + \gamma \epsilon_{\alpha\beta\gamma} S_\gamma^{(0)} \delta H_\beta(\omega) \\ &+ \frac{\Xi_{\alpha\lambda}}{i\omega} \delta S_\lambda(\omega) + \frac{C_{\alpha\eta}}{i\omega} \delta H_\eta(\omega) \end{aligned} \quad (65)$$

and

$$\begin{aligned} \Xi_{\alpha\lambda} &= \frac{\gamma^2}{\chi_\perp} K_{ij}^{ba} \Lambda_{ij\alpha\lambda}^{ba} + \frac{6g_D \gamma^2}{5\chi_\perp} R_{j\lambda\alpha\beta}^{db} Q_{\beta j}^{bd} + \frac{6g_D \gamma^2}{5\chi_\perp} V_\zeta^{d(0)} V_\gamma^{b(0)} \epsilon_{j\lambda\zeta} \epsilon_{\alpha\beta\gamma} Q_{\beta j}^{bd} \\ C_{\alpha\eta} &= \gamma G_{ij\alpha\eta}^{ba} K_{ij}^{ba} - \frac{6g_D \gamma}{5} R_{j\eta\alpha\beta}^{db} Q_{\beta j}^{bd} - \frac{6g_D \gamma}{5} V_\zeta^{d(0)} V_\gamma^{b(0)} \epsilon_{j\eta\zeta} \epsilon_{\alpha\beta\gamma} Q_{\beta j}^{bd}, \end{aligned} \quad (66)$$

where

$$\begin{aligned} R_{j\eta\alpha\beta}^{db} &= V_j^{d(0)} V_\beta^{b(0)} \delta_{\eta\alpha} - V_j^{d(0)} V_\alpha^{b(0)} \delta_{\eta\beta}, \\ G_{ij\alpha\gamma}^{ba} &= (\partial_i \partial_j V_\alpha^{b(0)}) V_\gamma^{a(0)} - (\partial_i \partial_j V_\beta^{b(0)}) \delta_{\beta\gamma} V_\alpha^{a(0)}, \\ \Lambda_{ij\alpha\lambda}^{ba} &= (\partial_i \partial_j V_\beta^{b(0)}) \delta_{\beta\lambda} V_\alpha^{a(0)} + (V_\gamma^{b(0)} V_\gamma^{a(0)} \delta_{\alpha\lambda} - \delta_{\gamma\lambda} V_\alpha^{b(0)} V_\gamma^{a(0)}) \partial_i \partial_j \\ &+ [(\partial_i V_\gamma^{b(0)}) V_\gamma^{a(0)} \delta_{\alpha\lambda} - (\partial_i V_\alpha^{b(0)}) V_\gamma^{a(0)} \delta_{\gamma\lambda}] \partial_j \\ &+ [(\partial_j V_\gamma^{b(0)}) V_\gamma^{a(0)} \delta_{\alpha\lambda} - (\partial_j V_\alpha^{b(0)}) V_\gamma^{a(0)} \delta_{\gamma\lambda}] \partial_i \\ &- \delta_{\gamma\lambda} (\partial_i \partial_j V_\alpha^{b(0)}) V_\gamma^{a(0)}. \end{aligned} \quad (67)$$

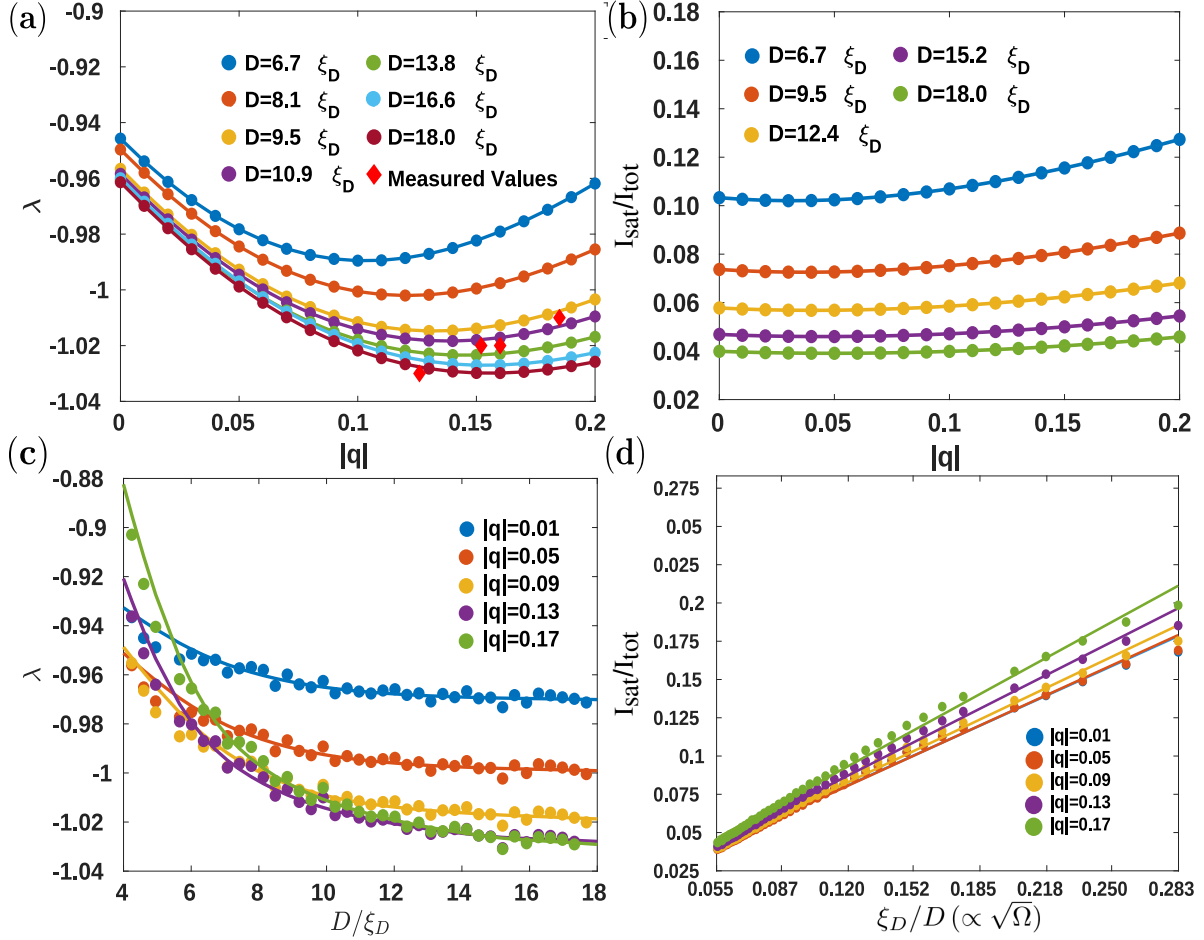


Figure 11. Transverse NMR frequency shift λ and relative soliton satellite intensity $I_{\text{sat}}/I_{\text{tot}}$ generated by inseparable spin solitons (π -solitons) [37]. The frequency shift λ is the lowest eigenvalue of Eq. (69) with the equilibrium texture of π -solitons in London limit. Filled circle represent the numeric results, while lines are smoothing splines. (a) Transverse NMR frequency shifts λ as functions of $|q|$ with different D . For large enough $D > 10\xi_D$, we find that λ decreases when $|q|$ increases as long as $|q| \leq 0.16$. The typical values of λ are around -1.015 to -1.03 . This agrees with experimental data from Ref. [40] (red diamonds). (b) Relative satellite intensity as a function of $|q|$. (c) Transverse NMR frequency shifts λ as a function of D . (d) Relative satellite intensity as a function of D .

The first two terms of Eq. (65) correspond to the NMR response of Larmor precession of δS_α with frequency $\omega_L = \gamma H^{(0)}$ and the last two terms of Eq. (65), known as torque terms, describe the NMR response related to the superfluid order parameter texture.

The torque terms in Eqs. (66) and (67) are fully determined by the equilibrium order parameter texture, i.e. the NMR frequency shift arises from the equilibrium texture of spin solitons. Taking the static magnetic field $\mathbf{H}^{(0)} = |\mathbf{H}^{(0)}|\hat{y}$ and the parametrization Eq. (36) into account, the poles of the dynamic response equations for the transverse spin density $\delta S_+ = \frac{1}{\sqrt{2}}[\delta S_1(\omega) + i\delta S_3(\omega)]$ under weak magnetic drive $\delta \mathbf{H}(t)$ become

$$(\omega^2 - \omega_L^2)\delta S_+(\omega) = (\Xi_{11} + \Xi_{33}) + i(\Xi_{13} - \Xi_{31})\delta S_+(\omega). \quad (68)$$

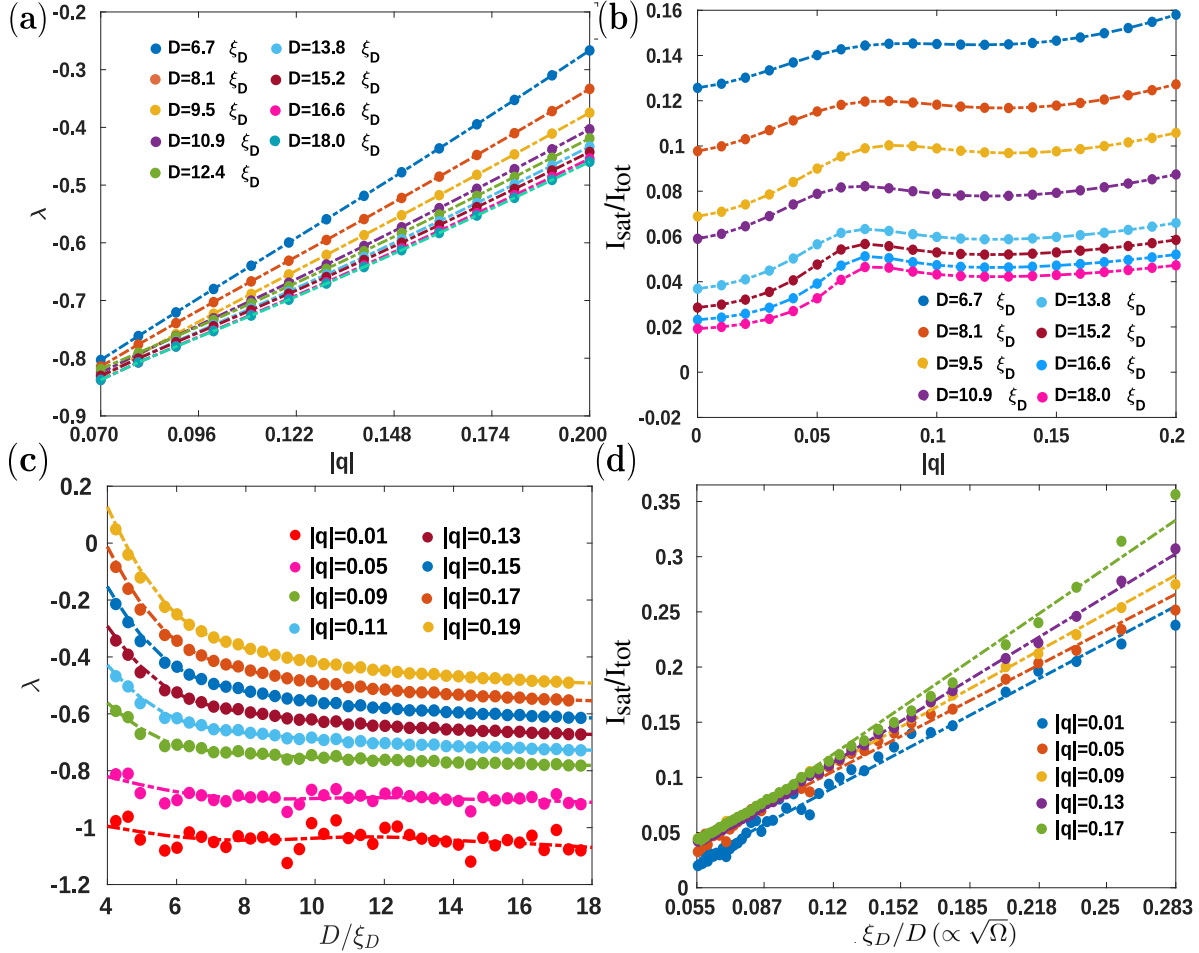


Figure 12. Transverse NMR frequency shift λ and relative soliton satellite intensity $I_{\text{sat}}/I_{\text{tot}}$ generated by separable spin solitons (KLS-solitons and solitons) [37]. The frequency shifts λ are eigenvalues of Eq. (69) with equilibrium textures of $1/4 + 1/4$ spin solitons in London limit. Filled circle represent the numeric results, while lines are smoothing splines. (a) Transverse NMR frequency shifts λ increases when $|q|$ increases. This is because only solitons ($|\Delta\theta| = \pi - 2\theta_0$) contribute to the lowest transverse spin dynamic response mode. When $|q|$ increases, λ generated by solitons increases. The typical values of λ are larger than -0.9 when $D \geq 10\xi_D$. (b) Relative satellite intensity as a function of $|q|$. (c) Transverse frequency shifts λ as a function of D . (d) Relative satellite intensity as a function of D .

In experiments, the observed transverse frequency shift λ is found from an eigen-equation using the parametrization in Eq. (36). For the full calculation, we refer the reader to Refs. [37, 62]. The end result of the calculations is

$$\begin{aligned} \lambda \delta S_+(\omega) = & \xi_D^2 [(6q_2^2 + q_1^2 + 1)\partial_y \partial_y + (3q_1^2 + 2q_2^2 + 1)\partial_x \partial_x] \delta S_+(\omega) \\ & - (2\xi_D^2 iV - U) \delta S_+(\omega) \end{aligned} \quad (69)$$

with

$$\begin{aligned} V = & (1 + 3q_1^2 \cos 2\theta) \partial_x \theta \partial_x + (1 + q_1^2) \partial_y \theta \partial_y \\ & + \frac{1}{2\xi_D^2} [(1 + q_1)^2 \sin 2\theta - (1 + q_1)q_2 \cos \theta], \end{aligned}$$

$$U = (1 + q_1)[-(1 + q_1) \cos 2\theta - 5q_2 \sin \theta] + 1 + q_1^2 + 4q_2^2, \quad (70)$$

and

$$\lambda = \frac{(\omega^2 - \omega_L^2)^2}{\Omega_{\text{PdB}}}, \quad \Omega_{\text{PdB}}^2 = \left(\frac{5\chi_{\perp}}{6\gamma^2 \Delta_P^2 g_D} \right)^{-1}, \quad (71)$$

where we introduced the Leggett frequency in the PdB phase Ω_{PdB} . The Eigen-equation (69) was solved through Galerkin Eigen-value method with a finite element mesh [37, 62, 63, 64]. The Eigenvalues λ resulting from stationary configuration of spin solitons are plotted in Figs. 11 and 12 as a function of $|q|$. The relative intensity of the soliton satellite, determined as the ratio of the area of the satellite I_{sat} to the total area I_{tot} under the absorption spectrum can be calculated using found eigenfunctions δS_+ as

$$\frac{I_{\text{sat}}}{I_{\text{tot}}} = n \frac{\left| \int \delta S_+ dV \right|^2}{\int |\delta S_+|^2 dV}, \quad (72)$$

where $n = D^{-2}/2$ is the density of the solitons. The numerical results for λ agree well with experimental observations, discussed in more detail in Sec. 5.4, while $I_{\text{sat}}/I_{\text{tot}}$ scales proportionally to $\sqrt{\Omega}$, also similar to the experiment.

5. Experimental observations

In many experiments, vortex-bound solitons result in observable signatures in the NMR spectrum, playing an integral role in distinguishing various topological and composite defects in superfluid phases of ^3He . This section aims to provide a review on the experimental observations of such defects to date, underlining the role of solitons that led to these observations.

5.1. Identification of the spin-mass vortex in $^3\text{He-B}$

Spin-mass vortices are formed in $^3\text{He-B}$ as a rare event in two different processes: When the front of the transition between A and B phases of superfluid ^3He sweeps through the rotating sample [56] or by the Kibble-Zurek mechanism [57]. Identification of the spin-mass vortex is based on the NMR spectrum.

Owing to spin-orbit interaction the NMR absorption in $^3\text{He-B}$ is shifted from the Larmor frequency by an amount $\Delta\nu$ which depends on the local orientation of the anisotropy axis $\hat{\mathbf{n}}$ with respect to the applied magnetic field \mathbf{H} . In the experiment in Fig. 13, the field is oriented along the rotation axis $\mathbf{\Omega}$, which is also the symmetry axis of the sample cylinder. At the soliton sheet $\hat{\mathbf{n}} \perp \mathbf{H}$ (Fig. 10), which produces the maximum possible frequency shift $\Delta\nu_{\text{max}}$. Everywhere else in the rotating cylinder the angle between $\hat{\mathbf{n}}$ and \mathbf{H} (and thus the frequency shift) is smaller: The cluster of vortex lines in the center of the container gives rise to absorption with frequency shifts close to zero. The annular region with vortex-free counterflow around the cluster is responsible for the large absorption maximum at $0.8 \Delta\nu_{\text{max}}$. The height of this peak decreases, when new vortex lines are added to the cluster or if rotation velocity decreased with given

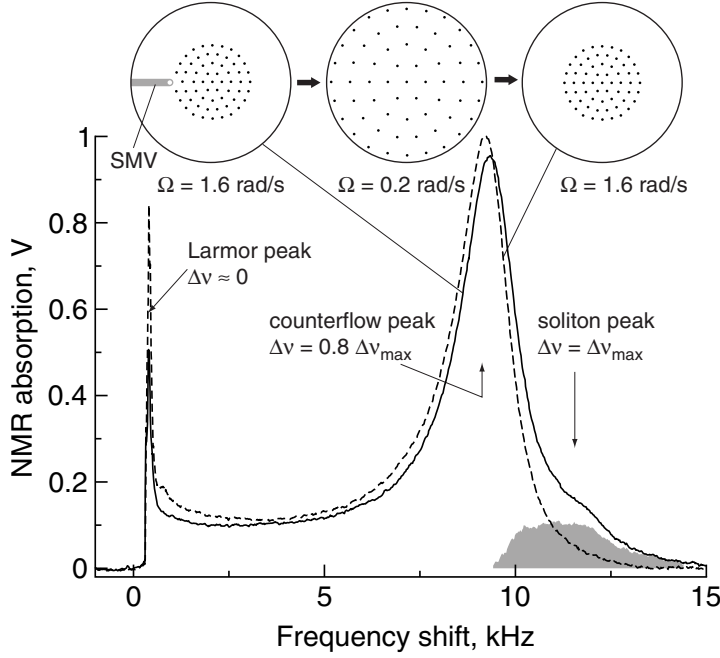


Figure 13. Spin-mass vortex in ${}^3\text{He-B}$ in the NMR observations [57].

number of vortices. The spectrum drawn with the solid line was measured after the neutron irradiation and shows the absorption from the soliton sheet, centered around $\Delta\nu_{\max}$. A top view of the rotating cylinder with the vortex cluster is depicted on the top row of the figure. This illustrates how the SMV can be selectively removed by reducing Ω to where the cluster has almost expanded to the wall (at 0.2 rad/s) and the SMV as the outermost vortex has been pushed to the cylinder wall. After increasing Ω back to the original 1.6 rad/s the spectrum plotted with the dashed line was recorded. The difference from the original spectrum is the absence of the soliton signal (shown by the gray area).

5.2. HQVs in the polar phase

In the polar phase, the sample regions where spin-orbit energy is at a minimum (i.e. in the volume not occupied by $\hat{\mathbf{d}}$ solitons) form the main peak in the NMR spectrum at the frequency [65]

$$\Delta\omega_{\text{P}} = \omega_{\text{P}} - \omega_{\text{L}} \approx \frac{\Omega_{\text{P}}^2}{2\omega_{\text{L}}} \cos^2 \mu. \quad (73)$$

Here Ω_{P} is the Leggett frequency in the polar phase, which characterizes the spin-orbit torque.

Winding of the $\hat{\mathbf{d}}$ vector, e.g. in the form of a soliton, provides an additional potential energy term for spin waves as the spin-orbit energy is not at minimum. Excitation of standing spin waves within these potential wells leads to a satellite peak

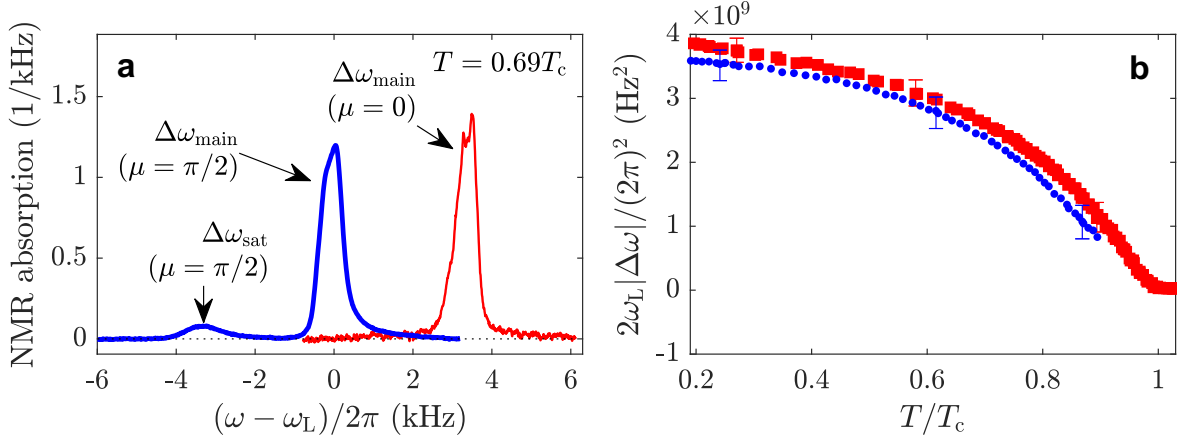


Figure 14. NMR spectra in the polar phase in the presence of HQVs. (a) Normalized spectra measured in transverse field $\mu = \pi/2$ (blue thick line) shows the HQV satellite at the negative frequency shift $\Delta\omega_{\text{Psat}}$ and the main line at zero frequency shift [39]. In the axial field $\mu = 0$ (red thin line) only the main line at positive shift $\Delta\omega_{\text{P}}$ is seen. This spectrum is not sensitive to presence of vortices as the spin-orbit interaction results in no trapping potential for spin waves. (b) Temperature dependencies of the satellite position in the transverse field $|\Delta\omega_{\text{Psat}}(\mu = \pi/2)|$ (blue circles) and the main line position in the axial field $\Delta\omega_{\text{P}}(\mu = 0)$ (red squares) closely match as expected for HQVs. The error bars show full width at half maximum of the main line as an estimate of possible systematic error.

in the NMR spectrum at frequency

$$\Delta\omega_{\text{Psat}} = \omega_{\text{Psat}} - \omega_{\text{L}} \approx \frac{\Omega_{\text{P}}^2}{2\omega_{\text{L}}} (\cos^2 \mu + \lambda_{\text{P}} \sin^2 \mu) , \quad (74)$$

where the parameter $\lambda_{\text{P}}(\mu)$ is specific to the type of the topological object. For example, an infinite planar $\hat{\mathbf{d}}$ soliton gives $\lambda_{\text{P}} = -1$ for the zero mode on the soliton [3, 65, 66]. The frequency shift for the satellite in this case becomes equal, but opposite than for the main peak, i.e. $\Delta\omega_{\text{Psat}}(\mu = \pi/2) = -\Delta\omega_{\text{P}}(\mu = 0)$. In reality, the finite soliton length (similar to Fig. 12c) and disorder in the nafen confinement may lead to reduced shift, and $|\lambda_{\text{P}}| < 1$ is expected [67]. In the experiments [39], a controlled amount of polarized HQVs was created by slowly cooling the sample in rotation with constant angular velocity Ω from above T_{c} in zero or axial (along $\hat{\Omega} \parallel \hat{\mathbf{m}}$) magnetic field. The presence of HQVs is apparent from the NMR spectrum via the related spin soliton peak, Fig. 14a. The experimental results, summarized in Fig. 14, indeed yield $\lambda_{\text{P}}(\mu = \pi/2) = -0.93 \pm 0.07$, in good agreement with theoretical expectations. We note that the predicted spin polarization of the HQV core [68] does not affect the signal, as the winding of the $\hat{\mathbf{d}}$ vector (and thus the spin polarization) is always opposite for a pair of HQVs connected by the spin soliton.

In the polar phase HQVs are energetically preferable to SQVs in axial or zero magnetic field [69, 70], Fig. 9. Application of tilted magnetic field changes the situation via the spin-orbit interaction related to winding of the $\hat{\mathbf{d}}$ vector within the HQV-bound spin solitons, making SQVs preferable to HQVs. In addition, SCVs can be created

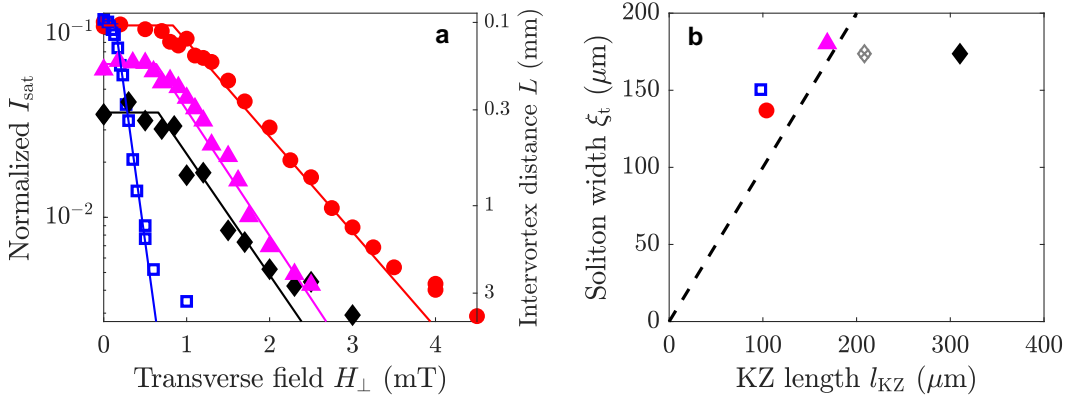


Figure 15. Suppression of the HQV density created by the KZM under a symmetry-breaking bias. **a** Filled red circles, magenta triangles, and black diamonds correspond to quench rates of $\tau_Q \approx 3.8 \cdot 10^2$ s, $\tau_Q \approx 1.4 \cdot 10^3$ s, and $\tau_Q \approx 7.7 \cdot 10^3$ s, respectively, while applying a constant $H = 11$ mT magnetic field [72]. The field is rotated to achieve different bias fields $H_{\perp} = H \sin \mu$. Open blue squares ($\tau_Q \approx 6.0 \cdot 10^2$ s) correspond to measurements with zero axial field component, $H_{\perp} = H$. Vortex density is constant for $H_{\perp} < H_{\perp t}$ and suppressed for higher bias fields. The suppression starts when the characteristic length scale of the bias field $\xi_{\text{bias}}(H_{\perp})$ becomes smaller than the relevant Kibble-Zurek length. Solid lines correspond to theoretical model (see text for details). The dashed line shows where the inter-vortex distance becomes comparable with the container size. **b** The extracted threshold bias length ξ_t as a function of l_{KZ} with the same symbols. The dashed line corresponds to $\xi_t = l_{\text{KZ}}$. The patterned gray diamond is the same measurement as the black diamond, but with l_{KZ} on the horizontal axis replaced with an estimation of the transition front thickness l_F [91]. For other measurements, l_F lies beyond the right border of the plot.

during the cooldown if strong time-dependent magnetic field is applied to generate a random distribution of vector $\hat{\mathbf{d}}$ [28, 30].

HQVs can be distinguished from SCVs by their connection to rotation. In particular, the dependence of the relative satellite peak intensity I_{sat} on the angular velocity Ω , shown in Fig. 17a, is expected to follow $\propto \sqrt{\Omega}$. This dependence follows from the following considerations; for solitons with their width set by the dipole length ξ_D , the expected signal intensity is $I_{\text{sat}} = (n_v/2) g_s L \xi_D$ [71]. Here $L = b n_v^{-1/2}$ is the average soliton length set by the average inter-vortex distance, while $g_s \sim 1$ and $b \sim 1$ are numerical factors. For a very low vortex density and long solitons $L \rightarrow \infty$ one has $g_s \rightarrow 2$. Since the vortex density $n_v \propto \Omega$, one expects $I_{\text{sat}} \propto \Omega^{1/2}$, as indeed confirmed in Fig. 17a.

In the experiments [39] with the magnetic field oriented transverse to the nafen strands during cooldown, the NMR satellite peak related to HQV-bound solitons was absent – consistent with creation of SQVs. The effect of the applied magnetic field on HQV creation was further studied in stationary (non-rotating) measurements in Ref. [72], where HQVs were created by temperature quenches via the Kibble-Zurek mechanism. The conclusion was that the HQV density is suppressed at the normal-polar phase transition when the soliton width, controlled by the magnetic field, becomes

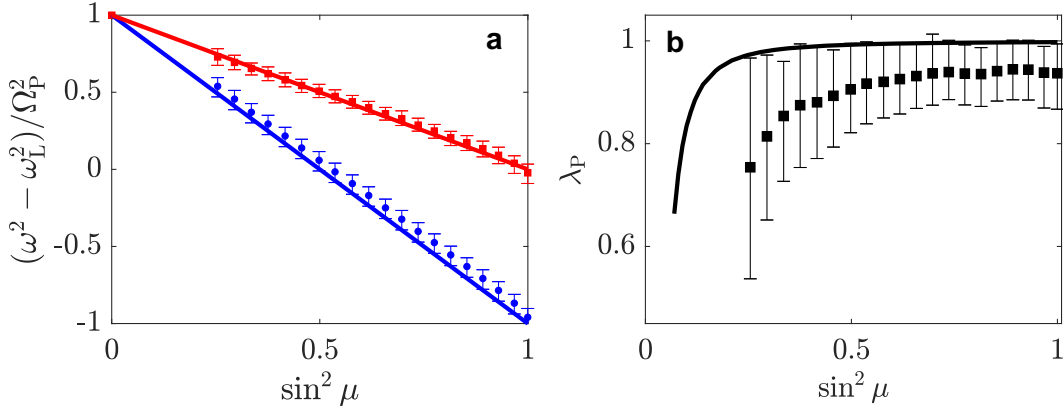


Figure 16. Frequency shift of the HQV satellite. (a) Measured values of the dimensionless frequency shift λ_P as a function of the field tilt angle μ (symbols) are compared with numerical calculations for the uniform polar phase (solid line) using theoretical value of $\xi_D = 17\mu\text{m}$ [39]. Leggett frequency Ω_P is determined from a separate measurement at $\mu = 0$. Deviation from the infinitely-long $\hat{\mathbf{d}}$ soliton value $\lambda_P = -1$ increases towards small μ . The disagreement between the experiment and calculations likely originates from disorder in the nafen strand orientation [67], which leads to fluctuations of the spin-orbit interaction energy within the solitons. (b) Values of λ_P are found from positions of the HQV satellite $\Delta\omega_{\text{Psat}}$ (blue circles) and of the main line $\Delta\omega_P$ (red squares). The red and blue solid lines show results of Eqs. (73) and (74), respectively, for $\lambda_P = -1$. The bars show full width at half maximum of the spectral lines in both panels.

smaller than the Kibble-Zurek length l_{KZ} , c.f. Fig. 15 and Eq. (75). One way to understand this observation is by assuming that the applied magnetic field then fixes the $\hat{\mathbf{d}}$ vector on a characteristic length scale defined by the magnetic field already during the phase transition. If the size of this length scale is smaller than the causally connected pockets created during the phase transition by the Kibble-Zurek mechanism, the $\hat{\mathbf{d}}$ vector orientation is correlated between the pockets – in contrast to the original idea assuming a random realization of the order parameter. Therefore, the very same properties that define the characteristic length scales of topological solitons also play an integral role in formation of topological defects during phase transitions.

Additionally, one might ask what is the interplay of the Kibble-Zurek mechanism (KZM) [73, 74] and rotation. The KZM is expected to create various order-parameter defects, including vortices of all possible types [75, 76, 77, 78]. In the transition, the inter-vortex distance is set by the KZ length

$$l_{\text{KZ}} = \xi_0(\tau_Q/\tau_0)^{1/4}, \quad (75)$$

where $\tau_Q^{-1} = -\frac{d(T/T_c)}{dt}\Big|_{T=T_c}$ is the cooldown rate at T_c , $\xi_0 = \xi(T = 0)$ and the order-parameter relaxation time $\tau_0 \sim 1\text{ ns}$. For HQVs the inter-vortex distance sets the length of the interconnecting solitons and thus the amplitude of the satellite signal. The resulting dependence $I_{\text{sat}} \propto n_v l_{\text{KZ}} \propto l_{\text{KZ}}^{-1} \propto \tau_Q^{-1/4}$ is indeed observed in the experiment, Fig. 17b. The magnitude of the signal corresponds to the averaged soliton length

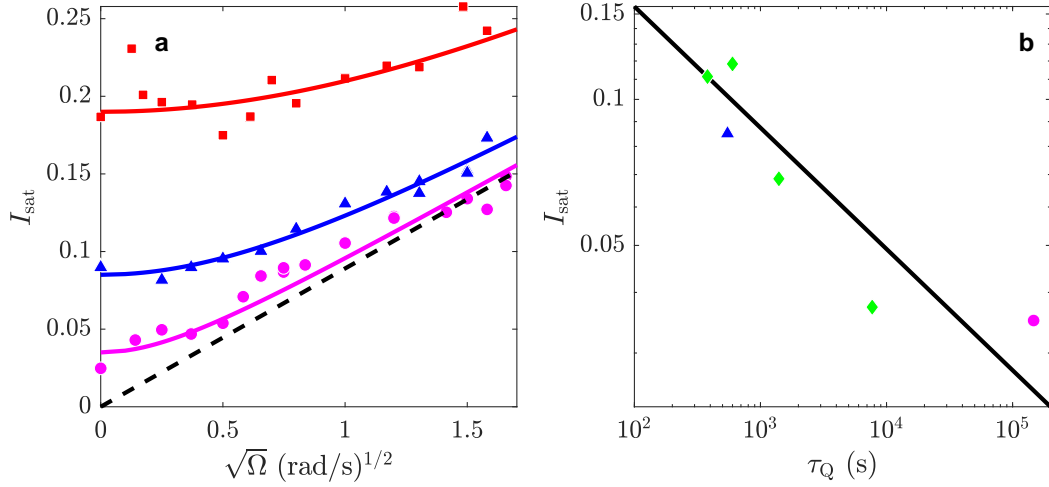


Figure 17. Intensity of the HQV satellite. **a** The satellite intensity I_{sat} measured in slow ($\tau_Q \approx 1.5 \cdot 10^5$ s, magenta circles) and fast ($\tau_Q \approx 5.5 \cdot 10^2$ s, blue triangles) zero-field cooldowns as a function of Ω . The solid lines are theoretical fits assuming that HQV creation by the KZM is independent from rotation. The dash line shows fitted equilibrium I_{sat} , corresponding to vanishing HQV density from KZM. Applying rf drive at the resonance during the cooldown in the axial field creates SCVs (red squares), seen as extra rotation-independent satellite intensity. **b** The satellite intensity I_{sat} measured in the absence of rotation and bias fields (green diamonds) follows the KZM power law $I_{\text{sat}} \propto \tau_Q^{-1/4}$ (solid line). The fitted satellite intensities at $\Omega = 0$ from panel **a** are marked with the corresponding symbols and colors.

of $1.4 l_{\text{KZ}}$, as has been estimated also in the B phase of ^3He [78, 79]. The shift of experimental data in Fig. 17a above the theoretical expectation indicates that the KZ mechanism is important also in cooldowns with applied rotation.

Observation of solitons bounded by HQVs, despite their positive tension, relies on a crucial experimental detail. Namely, the pinning of HQVs by the confining nafen strands is stronger than any relevant energy scale in the system. Each HQV core with a characteristic size given by the coherence length $\xi \sim 40$ nm, is penetrated by a few nafen strands of ~ 10 nm diameter. The strong pinning leads to effective pinning of HQVs in place right after their creation. For example, after stopping the rotation the satellite in the NMR spectrum remained unchanged for weeks, while the Magnus force, pulling vortices towards the sample boundary, exceeds the soliton tension by a large factor 10^3 .

Alternative method of observation of the solitons bounded by half-quantum vortices in the polar phase utilizes coherent magnetization precession state forming Bose-Einstein condensate of magnon quasiparticles, Fig. 18. The relaxation rate of magnon condensate increases proportionally to the volume occupied by the solitons. This method is especially useful with small amounts of solitons present in the sample, where accurate measurement of the satellite intensity in cw NMR might require an hour of averaging, relaxation rate can be measured with sufficient precision in seconds. At larger soliton densities, though, the relaxation rate becomes too fast to be reliably measured.

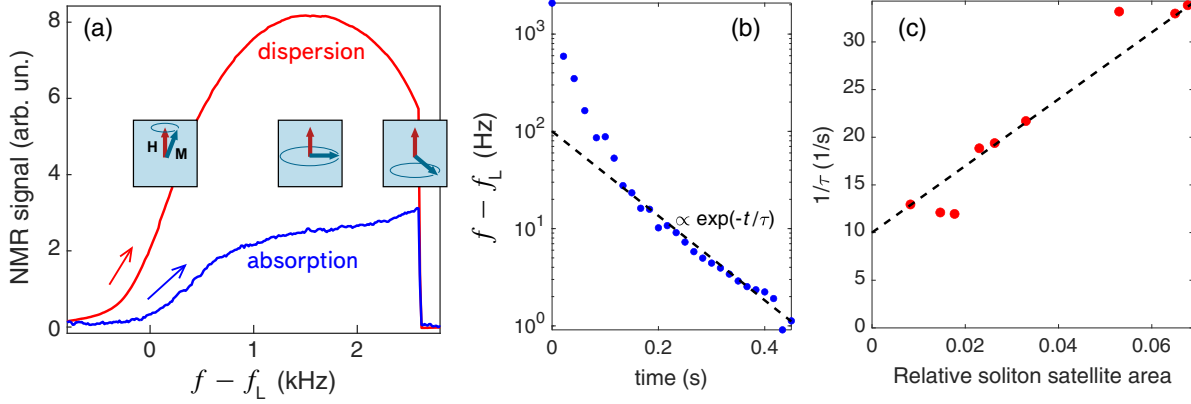


Figure 18. Detection of solitons bounded by half-quantum vortices in the polar phase using magnon BEC. (a) In continuous-wave NMR, coherently precessing magnetization state is formed with the sweep of the frequency of the pumping field f of sufficient magnitude via Larmor frequency f_L in the upward direction. It is manifested by a characteristic non-linear response. (b) When external pumping is switched off, the pumped magnons decay, but magnetization of the sample continues to precess coherently while the precession frequency f returns to f_L in exponential decay with time constant τ . (c) When solitons are present in the sample, the relaxation rate τ^{-1} increases proportionally to the volume occupied by the solitons, which is in the plot is characterized by the intensity of the soliton satellite in the NMR spectrum measured independently. The measurements are performed at $P = 7$ bar and $T = 0.4 T_c$ [92].

5.3. HQVs in the PdA phase

The transverse resonance frequency of the bulk fluid in the PdA phase with magnetic field in the direction parallel to the strand orientation, i.e. for $\mu = 0$, is [11]

$$\Delta\omega_{\text{PdA}} = \omega_{\text{PdA}} - \omega_L \approx \frac{\Omega_{\text{PdA}}^2}{2\omega_L}, \quad (76)$$

where Ω_{PdA} is the frequency of the longitudinal resonance in the PdA phase. The NMR line retains its shape during the second order phase transition from the polar phase but renormalizes the longitudinal resonance frequency due to appearance of the order parameter component with b .

Since the $\hat{\mathbf{m}}$ -vector is fixed by nafen parallel to the anisotropy axis, the $\hat{\mathbf{l}}$ -vector then lies on the plane perpendicular to it, prohibiting the formation of continuous vorticity [80] like the double-quantum vortex in $^3\text{He-A}$ [81]. Some planar structures in the $\hat{\mathbf{l}}$ -vector field, such as domain walls [82] or disclinations, remain possible but the effect of the $\hat{\mathbf{l}}$ -texture on the trapping potential for spin waves is negligible due to the large polar distortion [11] (i.e. for $b \ll 1$).

In the presence of HQVs the excitation of standing spin waves localized on the soliton leads to a characteristic NMR satellite peak in transverse ($\mu = \pi/2$) magnetic field, c.f. Fig. 19, with frequency shift

$$\Delta\omega_{\text{PdAsat}} = \omega_{\text{PdAsat}} - \omega_L \approx \lambda_{\text{PdA}} \frac{\Omega_{\text{PdA}}^2}{2\omega_L}, \quad (77)$$

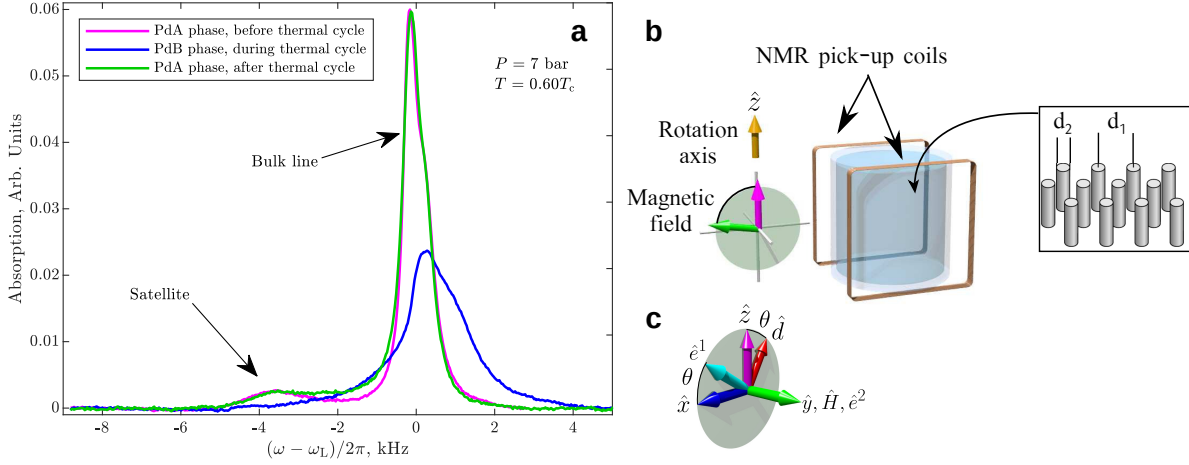


Figure 19. HQVs in thermal cycling. **a** The plot shows the measured NMR spectra in transverse ($\mu = \pi/2$) magnetic field in the presence of HQVs. HQVs were created by rotation with 2.5 rad/s during the transition from normal phase to the polar phase. The NMR spectrum includes the response of the bulk liquid and the $\hat{\mathbf{d}}$ -solitons, which appear as a characteristic satellite peak at lower frequency. The satellite intensity in the PdA phase remains unchanged after thermal cycling. The NMR spectrum in the PdB phase at the same temperature, measured between the two measurements in the PdA phase, is shown for reference [40]. **b** The ^3He sample is confined within a cylindrical container filled with commercially available nanomaterial called nafen-90 (where the number refers to its density in mg cm^{-3}) with uniaxial anisotropy, which consists of nearly parallel Al_2O_3 strands with $d_2 \approx 8$ nm diameter, separated by $d_1 \approx 50$ nm on average. The strands are oriented predominantly along the axis denoted $\hat{\mathbf{z}}$. The sample can be rotated with angular velocities up to 3 rad s^{-1} around the same axis. The sample is surrounded by rectangular nuclear magnetic resonance (NMR) pick-up coils. The static magnetic field transverse to the NMR coils can be oriented at an arbitrary angle μ with respect to the $\hat{\mathbf{z}}$ axis. **c** The magnetic field, oriented along the y -direction ($\mu = \pi/2$) in this figure, locks the $\hat{\mathbf{e}}^2$ -vector in the polar-distorted B phase order parameter, Eq. (16). Vectors $\hat{\mathbf{d}}$ and $\hat{\mathbf{e}}^1$ are free to rotate in the xz -plane by angle θ .

where λ_{PdA} is a dimensionless parameter dependent on the spatial profile (texture) of the order parameter across the soliton. For an infinite $\hat{\mathbf{d}}$ -soliton, one has $\lambda_{\text{PdA}} = -1$, corresponding to the zero-mode of the soliton, as in the polar phase [65, 66, 71, 83]. The measurements in the supercooled PdA phase, Fig. 19, at temperatures close to the transition to the PdB phase give value $\lambda_{\text{PdA}} \approx -0.9$, which is in good agreement with theoretical predictions and the polar phase measurements with the 243 mg/cm^3 nafen sample. This confirms that the structure of the $\hat{\mathbf{d}}$ -solitons connecting the HQVs is similar in polar and PdA phases and the effect of the orbital part to the trapping potential can be neglected. Furthermore, the satellite intensity shown in Fig 20 (b) scales with $\sqrt{\Omega}$ as in the polar phase, indicating that the observed signal is linked to topological solitons bounded by HQVs also in the PdA phase.

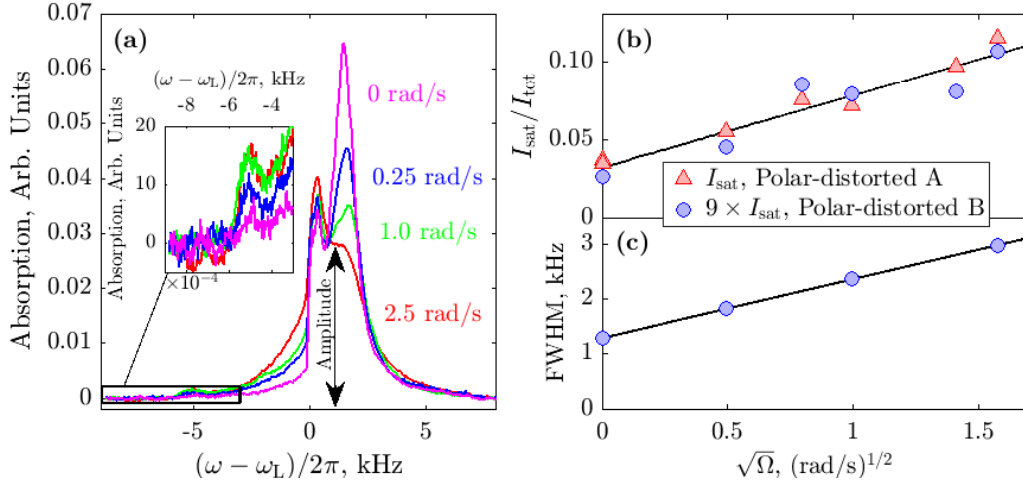


Figure 20. NMR spectra in the PdB phase. (a) The plot shows the measured NMR spectrum in the PdB phase at $0.38 T_c$ for different HQV densities, controlled by the angular velocity Ω at the time of crossing the T_c [40]. The presence of KLS walls produces characteristic features seen both as widening of the main line (located at small positive frequency shift) and as a satellite peak with a characteristic negative frequency shift. The inset shows magnified view of the satellite peak. (b) The satellite intensity in the PdA phase at $0.60T_c$ (blue circles) and in the PdB phase multiplied by a factor of 9 (red triangles) at $0.38T_c$ show the expected $\sqrt{\Omega}$ -scaling. The solid black line is a linear fit to the measurements including data from both phases. The non-zero $\Omega = 0$ intersection corresponds to vortices created by the Kibble-Zurek mechanism [73, 74, 39]. (c) The FWHM of the main line, determined from the spectrum in panel (a), gives $\text{FWHM} \approx 3$ kHz for 2.5 rad/s. FWHM for other angular velocities is recalculated from the amplitude of the main NMR line, shown in panel (a), assuming constant area.

5.4. Walls bounded by strings in the polar-distorted B phase

As established in Sec. 3.2, in the PdB isolated HQVs cease to be protected by topology in the PdB phase as the PdB phase lacks the relevant $\mathbb{Z}_2(\phi+\mathbf{s})$ symmetry. The experimental data, Fig. 19, strongly suggests the survival of HQVs in the phase transition to the PdB phase as composite defects, walls bounded by strings (or KLS walls), see Sec. 3.1. Let us now take a closer look at the experiments that led to this conclusion.

For a magnetic field oriented transverse to the uniaxial nafen anisotropy axis $\hat{\mathbf{z}}$, the order parameter of the PdB phase is given by Eq. (16). We denote with θ the rotation of the spin space with respect to the orbital space, with $\sin \theta_0 = q_2(2 - 2q_1)^{-1}$ corresponding to the minimum energy configuration for θ . The transverse frequency shift with uniform $\theta = \theta_0$ (i.e. the response of the bulk) is given as

$$\frac{\omega_{\perp}^2 - \omega_L^2}{\Omega_{\text{PdB}}^2} = q_1 - q_2^2. \quad (78)$$

This frequency shift was reported also in Ref. [16].

In the axial field, with \mathbf{H} oriented along the uniaxial anisotropy, the homogeneous

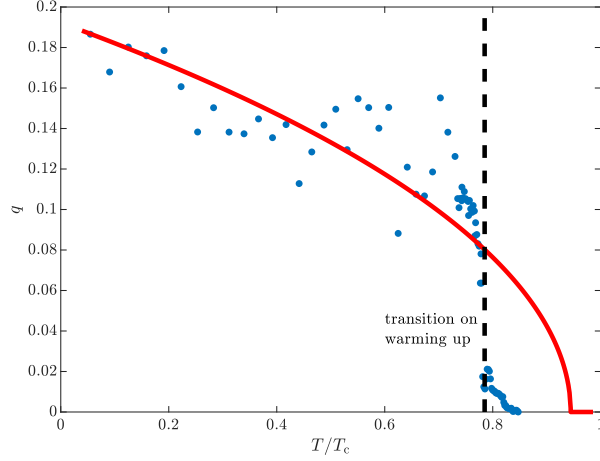


Figure 21. The measured distortion parameter q as a function of temperature. The dots represent the measured values for q . The solid red line is an estimation of q , calculated based on Ginzburg-Landau theory with strong-coupling corrections using two fitting parameters in the spirit of Ref. [16] and taking β parameter values from Ref. [93]. The PdB phase critical temperature is shown by dashed line for the transition to the PdA phase on warming. The jump in q at this temperature reflects the fact that the PdB-PdA transition is of the 1st order.

transverse frequency shift with uniform $\theta = \theta_{0,\parallel} = \text{sgn}(q_2)\pi/2$ is given as

$$\frac{\omega_{\parallel}^2 - \omega_{\text{L}}^2}{\Omega_{\text{PdB}}^2} = 1 + \frac{5}{2}|q_2|, \quad (79)$$

which is also equal to the value reported in Ref. [16].

The q -parameter value is determined from the frequency shifts in Eqs. (78) and (79), following a method described in Ref. [16]. In the experimental region of interest, the distortion factor is given by

$$q = \frac{2 - 5C}{4} - \frac{1}{4}\sqrt{25C^2 - 36C + 4}, \quad (80)$$

where

$$C = \frac{\omega_{\perp} - \omega_{\text{L}}}{\omega_{\parallel} - \omega_{\text{L}}}. \quad (81)$$

The expression (80) is valid in the range $q \in [0, (\sqrt{14}-2)/5]$. To measure q , we carefully prepare the state by cooling the sample through the superfluid transition temperature at zero rotation in the transverse magnetic field to avoid creation of half-quantum vortices. Then we cool the sample down to the lowest temperatures and start warming it up slowly, continuously monitoring the NMR spectrum. We perform two temperature sweeps, first in the axial and then in the transverse field. This way we can measure the q parameter in the coexistence region of the PdA and PdB phases. The results of our measurements are shown in Fig. 21.

In the transverse magnetic field \mathbf{H} exceeding the dipolar field ~ 3 mT, the order parameter vector $\hat{\mathbf{e}}^2$ in Eq. (16) becomes locked along the field, while vectors $\hat{\mathbf{d}}$ and $\hat{\mathbf{e}}^1$ are free to rotate around the axis $\hat{\mathbf{y}}$, directed along \mathbf{H} , with the angle θ between $\hat{\mathbf{d}}$ and

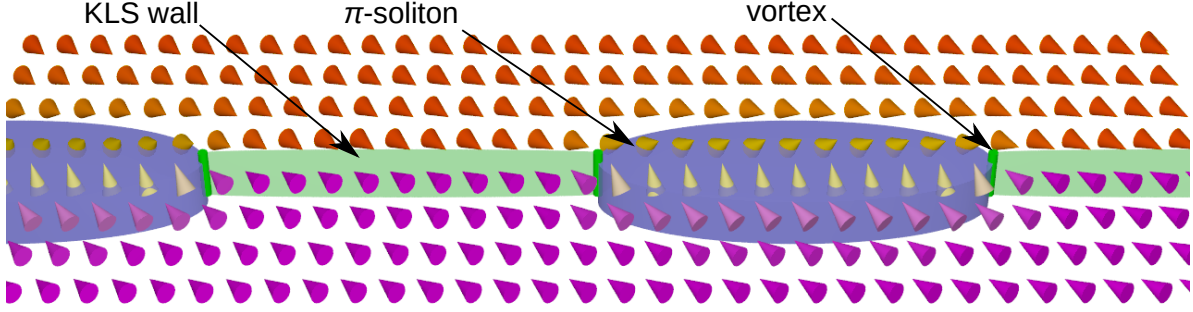


Figure 22. Composite defect of KLS wall and spin π -soliton connected by HQVs. Each HQV core terminates one soliton - reorientation of the spin part of the order parameter denoted by the angle θ - and one KLS wall. The orientation of the $\hat{\mathbf{d}}$ -vector is shown as cones where their color indicates the angle θ , based on numerical calculations. The π -soliton (blue), responsible for the observed NMR feature, corresponds to a situation where the KLS wall (light green) is bound between a different pair of HQV cores (green) than the soliton. The order parameter is continuous as the KLS walls are accompanied by virtual jumps, where $\phi \rightarrow \phi + \pi$, $\theta \rightarrow \theta + \pi$, and $q_2 \rightarrow -q_2$.

$\hat{\mathbf{z}}$. The order parameter of the PdB phase on a loop around a HQV has the following properties. The phase ϕ around the HQV core changes by π and the angle θ (and thus vectors $\hat{\mathbf{d}}$ and $\hat{\mathbf{e}}^1$) winds by π . Consequently, there is a phase jump $\phi \rightarrow \phi + \pi$ and related sign flips of vectors $\hat{\mathbf{d}}$ and $\hat{\mathbf{e}}^1$ along a perpendicular direction. In the presence of order-parameter components with $q > 0$, Eq. (16) remains single-valued if, and only if, q_2 also changes sign. We conclude that the resulting domain wall separates the degenerate states with $q_2 = \pm q$ and together with the bounding HQVs has a structure identical to the domain wall bounded by strings – the KLS wall – proposed by Kibble, Lazarides, and Shafi in cosmological context [44, 45] and discussed in details in Sec. 3.2.

The KLS wall and the topological soliton have distinct defining length scales [46, 84], see Fig. 4. The KLS wall has a hard core of the order of $q^{-1}\xi_0$ and the soliton has a soft core of the size of the dipole length $\xi_D \gg q^{-1}\xi_0$. The combination of these two objects may emerge in two different configurations, see Fig. 7. The observed frequency shift suggests the configuration, depicted in Fig. 22, where π -soliton and KLS wall connect at the HQV acting as nexus.

The appearance of KLS walls and the associated $\hat{\mathbf{d}}$ -solitons leads to a characteristic frequency shift

$$\Delta\omega_{\text{PdBSat}} = \omega_{\text{PdBSat}} - \omega_L \approx \lambda_{\text{PdB}} \frac{\Omega_{\text{PdB}}^2}{2\omega_L}, \quad (82)$$

The dimensionless parameter λ_{PdB} has been calculated in Sec. 4.1. Comparison of calculations with the experiment for all possible soliton structures from Fig. 6 is shown in Fig. 23. Numerical calculations give the low-temperature values $\lambda_{\text{soliton}} \sim -0.6$ for $\pi - 2\theta_0$ -soliton (“soliton”) and $\lambda_{\text{big}} \sim -1.5$ for its antisoliton, which has $\pi + 2\theta_0$ winding (“big soliton”). The $(2\theta_0)$ -soliton (“KLS soliton”) provides too shallow potential to have a spin-wave bound state distinguishable from the main line. The last possibility,

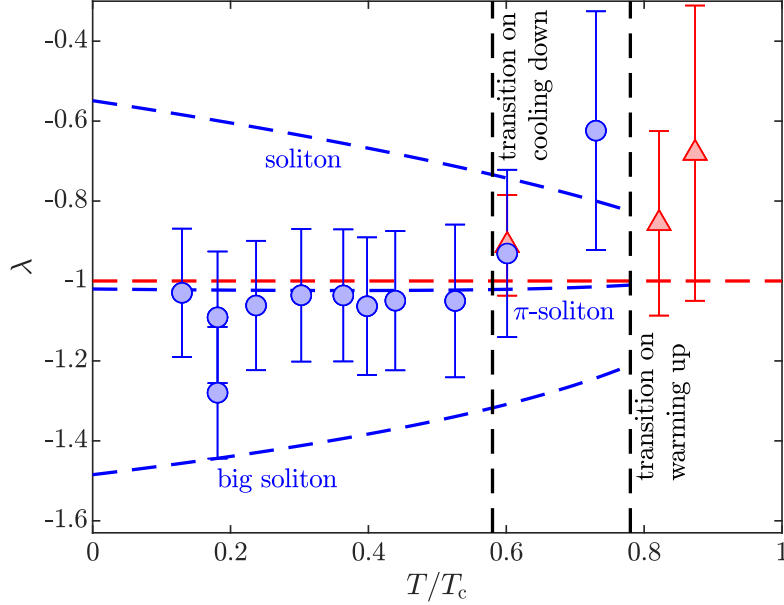


Figure 23. Frequency shift the HQV satellite as a function of temperature in the polar-distorted phases. In the PdA phase the measured values are in reasonable agreement with the theoretical prediction for a $\hat{\mathbf{d}}$ -soliton with π winding, shown as the red dashed line. The corresponding values in the PdB phase for the lowest-energy $\hat{\mathbf{d}}$ -soliton (soliton) and its antisoliton (big soliton), as well as the KLS soliton and the π -soliton (see text) are shown as dashed blue lines. The experimental data is taken from [40] and the dashed lines are based on 2D numerical calculations, Sec. 4.1, using $D = 20\xi_D$. The error bars denote the uncertainty in the position of the satellite peak by 1.0 kHz and 0.5 kHz in the PdB and PdA phases, respectively. The uncertainty is taken as the full width at half maximum (FWHM) of the satellite peak in the PdB phase and as half of the FWHM due to improved signal-to-noise ratio in the PdA phase.

the inseparable “ π -soliton”, gives $\lambda_\pi \approx -1$ for the accessible temperature range, in good agreement with the measured value, $\lambda_{\text{PdB}} \sim -1$. The measured values for λ_{PdB} , together with the fact that the total winding of the $\hat{\mathbf{d}}$ -vector is also equal to π in the PdA and polar phases above the transition temperature, suggest that the observed soliton structure in the PdB phase corresponds to the π -soliton in the presence of a KLS wall.

In addition, the KLS wall possesses a tension $\sim \xi q^2 \Delta_{\text{PdB}}^2 N_0$ [84, 85], where N_0 is the density of states. Thus the presence of KLS walls applies a force pulling the two HQVs at its ends towards each other. The fact that the number of HQVs remains unchanged in the phase transition signifies that the KLS wall tension does not exceed the maximum pinning force in the studied nafen sample. Strong pinning of single-quantum vortices in B-like phase in silica aerogel has also been observed previously [86]. An alternative way to remove a KLS wall is to create a hole within it, bounded by a HQV [44]. However, growth of such a HQV ring is also prohibited by the strong pinning by the nafen strands. We also note that for significantly larger values of q creation of a HQV vortex-antivortex pair within the KLS wall may become energetically favorable and as a result the HQV

pairs bounded by KLS walls would eventually shrink to singly-quantized vortices.

The satellite intensity in the PdB phase, c.f. Fig 20 (b), scales as $\sqrt{\Omega}$ – as in the polar and PdA phases. Although the scaling is identical, one striking difference appears in the PdB phase – the satellite intensity normalized to the total absorption integral in the PdB phase is smaller by a factor of ~ 9 compared to the PdA phase. Simultaneously, the original satellite intensity in the PdA phase is restored after a thermal cycle. There is currently no explanation for this observation.

Another effect of rotation in the PdB phase transverse ($\mu = \pi/2$) NMR spectrum is observed at the main peak, c.f. Fig. 20 (a). The full-width-at-half-maximum (FWHM), extracted from the amplitude of the main peak assuming $w \cdot h = \text{const}$, where w is its width and h is height, scales as $\propto \sqrt{\Omega}$; Fig. 20 (c). Increase in the FWHM may indicate that the presence of KLS walls enhances scattering of spin waves and thus results in increased dissipation. Alternatively, small negative frequency shift may originate from spin waves weakly bound between KLS walls.

6. Conclusions and outlook

In superfluid ^3He topological solitons are manifested as localized winding of the order parameter anisotropy vectors, connecting two energetically degenerate regions with one another. The soliton width is set by the magnetic or the spin-orbit coupling energy arising from deflection of the order parameter from the lowest-energy configuration within the soliton. The topological protection of the soliton structure is given by π_1 homotopy group, which is the same as for linear topological defects, quantized vortices. Thus solitons may terminate in bulk liquid on linear topological defects, in addition to possibility to terminate at the sample boundary. Vortices cores typically are of coherence length size, and are too small to be directly observed with the available experimental methods. Vortex-bound solitons provide an experimental tool for accessing properties of a range of exotic objects via NMR methods.

In this review article, we have shown the connection between solitons and the underlying order parameter symmetries, and how solitons are manifested in the experiments. So far experiments demonstrated three well-identified cases of solitons terminated at the quantized vortices: Solitons bounded by HQVs in the polar and PdA phases, solitons accompanying the KLS-walls in the PdB phase, and solitons connecting spin-mass vortices in the B phase of ^3He . The frequency shift of the associated feature in the NMR spectrum in all the cases agrees with theoretical predictions. This observation, together with the scaling of the soliton peak intensity with the angular velocity of the sample container confirmed the existence of HQVs [39] and of the spin-mass vortices [56]. The soliton peak has also been used to study Kibble-Zurek mechanism (KZM) of topological defect formation, in particular to demonstrate variety of defect types created by KZM [57] and to find modification of the KZM in the presence of a symmetry-breaking bias field [72], where the number of defects created in the phase transition was suppressed by applying magnetic field tilted with respect to the system symmetry axis during the

superfluid transition. In the PdB phase, the NMR properties of the spin soliton were used to identify the type of soliton accompanying KLS walls bounded by HQVs, where there were multiple possibilities [40, 37] with beautiful agreement achieved between calculations and measurement of the frequency shift of the soliton satellite. Recently, the effect of strong coupling correction on the domain wall structure in the superfluid B phase and the instability of domain wall induced by spin current in a spinor BEC was numerically studied [87, 88].

In conclusion, vortex-bound solitons are ubiquitous in different superfluid phases of ^3He . They have proven important for experimental identification of composite topological defects. Some composite topological defects, such as KLS walls bounded by strings, require a specific hierarchy of symmetry-breaking phase transitions in order to be realized. Simply proving their existence in the cosmological vacuum would be a major step forward in the study of the early times of our universe, immediately ruling out some grand unified theories [44]. Additionally, it has been proposed that solitons could provide observable signatures of axion dark matter [24]. Recently, topological classifications of Yang-Mills solitons, non-Abelian sine-Gordon solitons, and skyrmions in quantum field theories and quantum chromodynamics have also been discussed in terms of composite objects [89]. HQVs, identified by the NMR signature of the vortex-bound solitons, hold promise for topological, or error-tolerant, quantum computation with non-Abelian Majorana core-bound states [53]. Therefore, understanding and identifying vortex-bound solitons is important for a number of research directions.

Acknowledgments

We thank Grigori Volovik, Jaakko Nissinen and George Lazarides for useful discussions. This work was supported in part by Academy of Finland (grant 332964), by the European Union's Horizon 2020 research and innovation programme under Grant Agreement No. 824109, and by UK STFC grant number ST/T00682X/1.

Appendix A. Relative Homotopy Groups and Exact Sequences

The homotopy groups and relative homotopy groups of vacuum manifolds R_1 and R_2 form a long exact sequence (LES) [41]

$$\dots \pi_k(R_2) \xrightarrow{x_*^{n-1}} \pi_k(R_1) \xrightarrow{x_*^n} \pi_k(R_1, R_2) \xrightarrow{\partial^*} \pi_{k-1}(R_2) \dots \quad (\text{A.1})$$

The exact sequence of (relative) homotopy groups means that the image of any homomorphism $x_*^{n-1} : M \rightarrow N$ in Eq. (A.1) (the sets of the elements of the group N into which the elements of A are mapped) is the kernel of the next homomorphism $x_*^{n+1} : N \rightarrow W$ (the sets of the elements of N which are mapped to the zero or unit element of W) i.e. $\text{Im } x_*^n \cong \ker x_*^{n+1}$, with $n \in \mathbb{Z}$ [41].

The relative homotopy classes of $\pi_{k+1}(R_1, R_2)$ are mapped to the homotopy classes of $\pi_k(R_2)$ by mapping the k -dimensional subspace of $k + 1$ sphere, which surrounds

the defects, into R_2 . This mapping between two homotopy classes with different dimensions is called boundary homomorphism ∂^* [41]. When this mapping is not trivial, i.e. $\text{Im } \partial^* \neq 0$, topological defects given by $\pi_k(R_1, R_2)$ can be mapped to those given by $\pi_{k-1}(R_2)$, living on the $k+1$ sphere enclosing the original defects. In other words, boundary homomorphism describes how topological objects with different dimensionalities connect to one another – it is therefore a convenient tool for describing composite topological objects. In contrast, the commonly used homotopy group $\pi_k(R_1)$ lacks boundary homomorphism and therefore does not provide information about such connections.

The LES, Eq. (A.1), has infinite number of terms. It is therefore useful to split it up to short exact sequences (SES) [90]. For every relative homotopy group $\pi_1(R_1, R_2)$, the LES can be split as

$$0 \longrightarrow \text{Im } x_*^n \xrightarrow{x_*^n} \pi_k(R_1, R_2) \xrightarrow{\partial^*} \text{Im } \partial^* \longrightarrow 0 \quad (\text{A.2})$$

by the image of ∂^* and x_*^n . In this case, the relative homotopy group $\pi_k(R_1, R_2)$ is an extension of $\text{Im } x_*^n$ by $\text{Im } \partial^*$.

Appendix A.1. SESs of $\pi_n(R_1^{\text{PdA}}, R_2^{\text{PdA}})$

Following the definition of LES in Eq. (A.1) and the vacuum manifolds mentioned in Sec. 2.2, we have the LESs

$$\dots \pi_1(R_2^{\text{PdA}}) \xrightarrow{x_*^{n-1}} \pi_1(R_1^{\text{PdA}}) \xrightarrow{x_*^n} \pi_1(R_1^{\text{PdA}}, R_2^{\text{PdA}}) \xrightarrow{\partial_1^*} \pi_0(R_2^{\text{PdA}}) \dots \quad (\text{A.3})$$

and

$$\dots \pi_2(R_2^{\text{PdA}}) \xrightarrow{x_*^{n-1}} \pi_2(R_1^{\text{PdA}}) \xrightarrow{x_*^n} \pi_2(R_1^{\text{PdA}}, R_2^{\text{PdA}}) \xrightarrow{\partial_2^*} \pi_1(R_2^{\text{PdA}}) \dots, \quad (\text{A.4})$$

which in fact are

$$\dots \mathbb{Z}_{\mathbf{L}} \xrightarrow{x_*^{n-1}} \mathbb{Z}_{\mathbf{L}} \times \mathbb{Z}_\phi \xrightarrow{x_*^n} \pi_1(R_1^{\text{PdA}}, R_2^{\text{PdA}}) \xrightarrow{\partial_1^*} 0 \dots \quad (\text{A.5})$$

and

$$\dots 0 \xrightarrow{x_*^{n-1}} \mathbb{Z}_{\mathbf{S}} \xrightarrow{x_*^n} \pi_2(R_1^{\text{PdA}}, R_2^{\text{PdA}}) \xrightarrow{\partial_2^*} \mathbb{Z}_{\mathbf{L}} \dots \quad (\text{A.6})$$

It is easy to see that in Eq. (A.5) $\text{Im } \partial_1^* = 0$, while $\text{Im } x_*^{n-1} = \mathbb{Z}_{\mathbf{L}}$ as the orbital vertices formed by $\hat{\mathbf{n}}$ (or $\hat{\mathbf{l}} = \hat{\mathbf{m}} \times \hat{\mathbf{n}}$) form same group $\mathbb{Z}_{\mathbf{L}}$. It follows that $\ker x_*^n \cong \mathbb{Z}_{\mathbf{L}}$ and

$$\text{Im } x_*^n \cong (\mathbb{Z}_{\mathbf{L}} \times \mathbb{Z}_\phi) / \mathbb{Z}_{\mathbf{L}} = \mathbb{Z}_\phi, \quad (\text{A.7})$$

leading to the SES of $\pi_1(R_1^{\text{PdA}}, R_2^{\text{PdA}})$

$$0 \longrightarrow \mathbb{Z}_\phi \longrightarrow \pi_1(R_1^{\text{PdA}}, R_2^{\text{PdA}}) \xrightarrow{\partial^*} 0 \longrightarrow 0. \quad (\text{A.8})$$

Following similar reasoning, we have $\text{Im } \partial_2^* = 0$, where 0 is the kernel of the mapping $x_*^{n-1} : \mathbb{Z}_{\mathbf{L}} \mapsto \mathbb{Z}_{\mathbf{L}} \times \mathbb{Z}_\phi$, resulting in

$$0 \longrightarrow \mathbb{Z}_{\mathbf{S}} \longrightarrow \pi_2(R_1^{\text{PdA}}, R_2^{\text{PdA}}) \xrightarrow{\partial^*} 0 \longrightarrow 0. \quad (\text{A.9})$$

Appendix A.2. SESs of $\pi_n(R_1^{\text{PdB}}, R_2^{\text{PdB}})$

We now conduct the calculations of SESs for the PdB phase. Similarly to the previous section, we start from

$$\dots \mathbb{Z}_{\mathbf{J}} \xrightarrow{x_*^{n-1}} \mathbb{Z}_{2\mathbf{J}} \times \mathbb{Z}_\phi \xrightarrow{x_*^n} \pi_1(R_1^{\text{PdB}}, R_2^{\text{PdB}}) \xrightarrow{\partial_1^*} \mathbb{Z}_{2(\phi+\mathbf{S})} \longrightarrow 0 \dots \quad (\text{A.10})$$

and

$$\dots 0 \xrightarrow{x_*^{n-1}} 0 \longrightarrow \pi_2^*(R_1^{\text{PdA}}, R_2^{\text{PdA}}) \xrightarrow{\partial_2^*} \mathbb{Z}_{\mathbf{J}} \xrightarrow{x_*^{n+1}} \mathbb{Z}_\phi \times \mathbb{Z}_{2\mathbf{J}} \dots, \quad (\text{A.11})$$

where

$$\mathbb{Z}_{\mathbf{J}} = \pi_1(R_2^{\text{PdB}}), \mathbb{Z}_\phi \times \mathbb{Z}_{2\mathbf{J}} = \pi_1(R_1^{\text{PdB}}), 0 = \pi_0(R_2^{\text{PdB}}) = \pi_0(R_1^{\text{PdB}}). \quad (\text{A.12})$$

Mapping $x_*^{n-1} : \pi_1(R_2^{\text{PdB}}) \mapsto \pi_1(R_1^{\text{PdB}})$ (x_*^{n+1} in Eq. (A.11)) plays a significant role in splitting Eqs. (A.10) and (A.11). The $\mathbb{Z}_{\mathbf{J}}$ vertices are mapped into $\mathbb{Z}_{2\mathbf{J}}$ through a surjection, i.e. $\text{Im } x_*^{n-1} = \mathbb{Z}_{\mathbf{J}}$. A natural choice of $\ker x_*^{n-1}$ is $2\mathbb{Z}_{\mathbf{J}}$, which is a group of vortices with even winding number [36]. As a result, $\text{Im } \partial^*$ in Eqs. (A.10) and (A.11) are $\mathbb{Z}_{2(\phi+\mathbf{S})}$ and $2\mathbb{Z}_{\mathbf{J}}$, respectively. Since $\text{Im } x_*^{n-1} = \mathbb{Z}_{2\mathbf{J}} = \ker x_*^n$ in Eq. (A.10), we also have

$$\text{Im } x_*^n = (\mathbb{Z}_{2\mathbf{J}} \times \mathbb{Z}_\phi) / \ker x_*^n = \mathbb{Z}_\phi. \quad (\text{A.13})$$

Then we get the SES

$$0 \longrightarrow \mathbb{Z}_\phi \longrightarrow \pi_1(R_1^{\text{PdB}}, R_2^{\text{PdB}}) \xrightarrow{\partial^*} \mathbb{Z}_{2(\phi+\mathbf{S})} \longrightarrow 0 \quad (\text{A.14})$$

for $\pi_1(R_1^{\text{PdB}}, R_2^{\text{PdB}})$ and

$$0 \longrightarrow 0 \longrightarrow \pi_2(R_1^{\text{PdB}}, R_2^{\text{PdB}}) \xrightarrow{\partial^*} 2\mathbb{Z}_{\mathbf{J}} \longrightarrow 0 \quad (\text{A.15})$$

for $\pi_2(R_1^{\text{PdB}}, R_2^{\text{PdB}})$.

Appendix A.3. SES of $\pi_1(R_1^{\text{H}}, \tilde{R}_1^{\text{SOC}})$

The long exact sequence for $\pi_1(R_1^{\text{H}}, \tilde{R}_1^{\text{SOC}})$ with reduced vacuum manifolds is written as

$$\pi_1(\tilde{R}_1^{\text{SOC}}) \longrightarrow \pi_1(R_1^{\text{H}}) \xrightarrow{x_*^n} \pi_1(R_1^{\text{H}}, \tilde{R}_1^{\text{SOC}}) \xrightarrow{\partial^*} \pi_0(\tilde{R}_1^{\text{SOC}}) \longrightarrow \pi_0(R_1^{\text{H}}), \quad (\text{A.16})$$

where ∂^* is the boundary homomorphism [41, 90]. Plugging in the homotopy groups of the reduced manifold, Eq. (A.16), gives

$$\mathbb{Z}_\phi \longrightarrow \mathbb{Z}_{\mathbf{S}} \times \mathbb{Z}_\phi \xrightarrow{x_*^n} \pi_1(R_1^{\text{H}}, \tilde{R}_1^{\text{SOC}}) \xrightarrow{\partial^*} \mathbb{Z}_4 \longrightarrow 0. \quad (\text{A.17})$$

It is worth noting that $\text{Im } \partial^* = \mathbb{Z}_4$ and $\text{Im } x_*^n = \mathbb{Z}_{\mathbf{S}}$, resulting in

$$0 \longrightarrow \mathbb{Z}_{\mathbf{S}} \xrightarrow{x_*^n} \pi_1(R_1^{\text{H}}, \tilde{R}_1^{\text{SOC}}) \xrightarrow{\partial^*} \mathbb{Z}_4 \longrightarrow 0. \quad (\text{A.18})$$

[1] L. D. Landau, *The Theory of a Fermi Liquid*, J. Exptl. Theoret. Phys. (U.S.S.R.) **30**, 1058 (1956).

[2] J. Bardeen, L. N. Cooper, and J. R. Schrieffer, *Microscopic Theory of Superconductivity*, Phys. Rev. **106**, 162 (1957).

[3] D. Vollhardt and P. Wölfle, *The Superfluid Phases of Helium 3* (Dover, 2013).

- [4] T. Mizushima, Y. Tsutsumi, M. Sato, and K. Machida, *Symmetry protected topological superfluid $^3\text{He-B}$* , Journal of Physics: Condensed Matter **27**, 113203 (2015).
- [5] V.P. Mineyev and G.E. Volovik, *Planar and linear solitons in superfluid ^3He* , Phys. Rev. B. **18**, 3197 (1978).
- [6] A. J. Leggett, *A theoretical description of the new phases of liquid ^3He* , Rev. Mod. Phys. **47**, 331 (1975).
- [7] N. Zhelev, T. S. Abhilash, E. N. Smith, R. G. Bennett, X. Rojas, L. Levitin, J. Saunders, and J. M. Parpia, *The A-B transition in superfluid helium-3 under confinement in a thin slab geometry*, Nat. Commun. **8**, 15963 (2017).
- [8] L. V. Levitin, R. G. Bennett, A. Casey, B. Cowan, J. Saunders, D. Drung, T. Schurig, and J. M. Parpia, *Phase Diagram of the Topological Superfluid ^3He Confined in a Nanoscale Slab Geometry*, Science **340**, 841 (2013).
- [9] J. I. A. Li, A. M. Zimmerman, J. Pollanen, C. A. Collett, W. J. Gannon, and W. P. Halperin, *Stability of Superfluid $^3\text{He-B}$ in Compressed Aerogel*, Phys. Rev. Lett. **112**, 115303 (2014).
- [10] J. J. Wiman and J. A. Sauls, *Superfluid Phases of ^3He in a Periodic Confined Geometry*, J. Low Temp. Phys. **175**, 17 (2014).
- [11] V. V. Dmitriev, A. A. Senin, A. A. Soldatov, and A. N. Yudin, *Polar Phase of Superfluid ^3He in Anisotropic Aerogel*, Phys. Rev. Lett. **115**, 165304,(2015).
- [12] R. S. Askhadullin, V. V. Dmitriev, D. A. Krasnikhin, P. N. Martynov, A. A. Osipov, A. A. Senin, and A. N. Yudin, *Phase diagram of superfluid ^3He in “nematically ordered” aerogel*, JETP Letters **95**, 326 (2012).
- [13] S. Yang and R. Ikeda, *Possibility of Unconventional Pairing States in Superfluid ^3He in Uniaxially Anisotropic Aerogels*, Journal of the Physical Society of Japan **83**, 084602 (2014).
- [14] I. A. Fomin, *Analog of Anderson theorem for the polar phase of liquid ^3He in nematic aerogel*, JETP **127**, 933 (2018).
- [15] T. Kamppinen, J. Rysti, M.-M. Volard, G.E. Volovik, and V.B. Eltsov, *Topological nodal line in superfluid ^3He and the Anderson theorem*, arXiv:1908.01645v4 (2022).
- [16] V. V. Dmitriev, A. A. Senin, A. A. Soldatov, E. V. Surovtsev, and A. N. Yudin, *B phase with polar distortion in superfluid ^3He in “ordered” aerogel*, JETP **119**, 1088, (2014).
- [17] G. Lazarides, Q. Shafi, *Axion models with no domain wall problem*, Phys. Lett. B **115**, 21 (1982).
- [18] G. Lazarides, Q. Shafi, *Monopoles, strings, and necklaces in $SO(10)$ and $E6$* , J. High Energ. Phys. **2019**, 193 (2019).
- [19] G. Lazarides, Q. Shafi, *Triply charged monopole and magnetic quarks*, Phys. Lett. B **818**, 136363 (2021).
- [20] G. Lazarides, Q. Shafi, *Dirac plus Nambu monopoles in the Standard Model*, Phys. Rev. D **104**, 035020 (2021)
- [21] M. Nitta, *Confinement and moduli locking of Alice strings and monopoles*, J. High Energ. Phys. **2021**, 276 (2021).
- [22] M. Nitta, *Non-Abelian Alice strings in two-flavor dense QCD*, Phys. Rev. D **103**, 054002 (2021).
- [23] S. Ryosuke, T. Fuminobu and Y. Masaki, *Unified origin of axion and monopole dark matter, and solution to the domain-wall problem*, Phys. Rev. D **98**, 043535 (2018).
- [24] D. J. E. Marsh and A.-R. Pop *Axion dark matter, solitons and the cusp-core problem*, Mon. Notices Royal Astron. Soc. **451**, 2479 (2015).
- [25] I. Martin Isaacs, *Algebra: A Graduate Course* (American Mathematical Society, 2009).
- [26] M. Nakahara, *Geometry, Topology and Physics* (CRC Press, 2003).
- [27] G. E. Volovik, *Monopoles and fractional vortices in chiral superconductors*, Proc. Nat. Acad. Sci. **97**, 2431 (2000).
- [28] V.V. Dmitriev, D.A. Krasnikhin, N. Mulders, A.A. Senin, G.E. Volovik, A.N. Yudin, *Orbital glass and spin glass states of $^3\text{He-A}$ in aerogel*, JETP Lett. **91**, 599 (2010).
- [29] J.I.A. Li, J. Pollanen, A.M. Zimmerman, C.A. Collett, W.J. Gannon, W.P. Halperin, *The superfluid glass phase of $^3\text{He-A}$* , Nat. Phys. **9**, 775 (2013).

- [30] G. E. Volovik, J. Rysti, J. T. Mäkinen, and V. B. Eltsov, *Spin, orbital, Weyl and other glasses in topological superfluids*, J. Low Temp. Phys. **196**, 73 (2019).
- [31] V.V. Dmitriev, A.A. Soldatov, and A.N. Yudin, *Superfluid ^3He in a nematic aerogel*, JETP **131**, 2 (2020).
- [32] L.V. Levitin, B. Yager, L. Sumner, B. Cowan, A.J. Casey, J. Saunders, N. Zhelev, R.G. Bennett, and J.M. Parpia, *Evidence for a Spatially Modulated Superfluid Phase of ^3He under Confinement*, Phys. Rev. Lett. **122**, 085301 (2019).
- [33] P. M. Walmsley, I. J. White, and A. I. Golov, *Intrinsic Pinning of Vorticity by Domain Walls of \hat{l} Texture in Superfluid $^3\text{He-A}$* , Phys. Rev. Lett. **93**, 195301 (2004).
- [34] H. Ikegami, Y. Tsutsumi, and K. Kono, *Observation of Intrinsic Magnus Force and Direct Detection of Chirality in Superfluid $^3\text{He-A}$* , J. Phys. Soc. Jpn. **84**, 044602 (2015).
- [35] J. Kasai, Y. Okamoto, K. Nishioka, T. Takagi, and Y. Sasaki, *Chiral Domain Structure in Superfluid $^3\text{He-A}$ Studied by Magnetic Resonance Imaging*, Phys. Rev. Lett. **120**, 205301 (2018).
- [36] G. E. Volovik and K. Zhang, *String monopoles, string walls, vortex skyrmions, and nexus objects in the polar distorted B phase of ^3He* , Phys. Rev. Research **2**, 023263 (2020).
- [37] K. Zhang, *One-dimensional nexus objects, network of Kibble-Lazarides-Shafi string walls, and their spin dynamic response in polar-distorted B-phase of ^3He* , Phys. Rev. Research **2**, 043356 (2020).
- [38] G. E. Volovik, *The Universe in a Helium Droplet* (Oxford, 2009).
- [39] S. Autti, V. V. Dmitriev, J. T. Mäkinen, A. A. Soldatov, G. E. Volovik, A. N. Yudin, V. V. Zavjalov, and V. B. Eltsov, *Observation of Half-Quantum Vortices in Topological Superfluid ^3He* , Phys. Rev. Lett. **117**, 255301 (2016).
- [40] J. T. Mäkinen, V. V. Dmitriev, J. Nissinen, J. Rysti, G. E. Volovik, A. N. Yudin, K. Zhang, and V. B. Eltsov, *Half-quantum vortices and walls bounded by strings in the polar-distorted phases of topological superfluid ^3He* , Nat. Commun. **10**, 237 (2019).
- [41] C. Nash and S. Sen, *Topology and Geometry for Physicists* (Academic Press, 1988).
- [42] S. Kang, S. W. Seo, H. Takeuchi, and Y. Shin, *Observation of Wall-Vortex Composite Defects in a Spinor Bose-Einstein Condensate*, Phys. Rev. Lett. **122**, 095301 (2019).
- [43] I-K. Liu, S.-C. Gou, and H. Takeuchi, *Phase diagram of solitons in the polar phase of a spin-1 Bose-Einstein condensate*, Phys. Rev. Research **2**, 033506 (2020).
- [44] T. W. B. Kibble, G. Lazarides, and Q. Shafi, *Walls bounded by strings*, Phys. Rev. D **26**, 435 (1982).
- [45] T. Kibble, G. Lazarides, and Q. Shafi, *Strings in $SO(10)$* , Phys. Lett. B **113**, 237 (1982).
- [46] G. E. Volovik, *Half quantum vortices in the B phase of superfluid ^3He* , JETP Lett. **52**, 358 (1990).
- [47] V. P. Mineyev and G. E. Volovik, *Planar and linear solitons in superfluid ^3He* , Phys. Rev. B **18**, 3197 (1978).
- [48] G. E. Volovik and V. P. Mineev, *Line and point singularities in superfluid ^3He* , JETP Lett. **24**, 593 (1976).
- [49] J. R. Kirtley, C. C. Tsuei, M. Rupp, J. Z. Sun, L. S. Yu-Jahnes, A. Gupta, M. B. Ketchen, K. A. Moler, and M. Bhushan, *Direct Imaging of Integer and Half-Integer Josephson Vortices in High- T_c Grain Boundaries*, Phys. Rev. Lett. **76**, 1336, (1996).
- [50] J. Jang, D. G. Ferguson, V. Vakaryuk, R. Budakian, S. B. Chung, P. M. Goldbart, and Y. Maeno, *Observation of Half-Height Magnetization Steps in Sr_2RuO_4* , Science **331**, 186 (2011).
- [51] K. G. Lagoudakis, T. Ostatnický, A. V. Kavokin, Y. G. Rubo, R. André, and B. Deveaud-Plédran, *Observation of Half-Quantum Vortices in an Exciton-Polariton Condensate*, Science **326**, 974 (2009).
- [52] S. W. Seo, S. Kang, W. J. Kwon, and Y.-i. Shin, *Half-Quantum Vortices in an Antiferromagnetic Spinor Bose-Einstein Condensate*, Phys. Rev. Lett. **115**, 015301 (2015).
- [53] D. A. Ivanov, *Non-Abelian Statistics of Half-Quantum Vortices in p-Wave Superconductors*, Phys. Rev. Lett. **86**, 268 (2001).
- [54] A. Kitaev, *Fault-tolerant quantum computation by anyons*, Annals of Physics **303**, 2 (2003).
- [55] F. Zhou, *Spin Correlation and Discrete Symmetry in Spinor Bose-Einstein Condensates*, Phys.

- Rev. Lett. **87**, 080401 (2001).
- [56] Y. Kondo, J.S Korhonen, M. Krusius, V.V. Dmitriev, E.V. Thuneberg, and G.E. Volovik, *Combined spin-mass vortices with soliton tail in superfluid $^3\text{He-B}$* , Phys. Rev. Lett. **68**, 3331 (1992).
- [57] V.B. Eltsov, T.W.B. Kibble, M. Krusius, V.M.H. Ruutu and G.E. Volovik, *Composite Defect Extends Analogy between Cosmology and ^3He* , Phys. Rev. Lett. **85**, 4739 (2000).
- [58] P. W. Anderson, *Some Macroscopic Considerations on Motions of Anisotropic Superfluids*, Phys. Rev. Lett. **30**, 368 (1973).
- [59] P. W. Anderson and C. M. Varma, *Properties of a Possible Superfluid State of ^3He* , Nature **241**, 187 (1973).
- [60] P. M. Chaikin, *Principles of Condensed Matter Physics* (Cambridge University Press, 1995).
- [61] I. E. Dzyaloshinskii and G. E. Volovick, *Poisson brackets in condensed matter physics*, Annals of Physics **125**, 67 (1980).
- [62] K. Zhang, PhD degree thesis, *Cosmological Composite Topological Defects in Uniaxially Disordered Superfluid ^3He* , University of Helsinki (2021).
- [63] K. Zhang, *Code for the nexus-soliton calculations*, https://quank-hpc.github.io/nexus_soliton.html (2021).
- [64] S. C. Brenner and L. R. Scott, *The Mathematical Theory of Finite Element Methods*, (Springer New York, 2008)
- [65] V. P. Mineev, *NMR Properties of the Polar Phase of Superfluid ^3He in Anisotropic Aerogel Under Rotation*, J Low Temp. Phys. **184**, 1007 (2016).
- [66] V. V. Zavjalov, *Linear NMR in the polar phase of ^3He in aerogel*, JETP Lett. **108**, 402 (2018).
- [67] V. E. Asadchikov, R. S. Askhadullin, V. V. Volkov, V. V. Dmitriev, N. K. Kitaeva, P. N. Martynov, A. A. Osipov, A. A. Senin, A. A. Soldatov, D. I. Chekrygina, and A. N. Yudin, *Structure and properties of “nematically ordered” aerogels*, JETP Lett. **101**, 556 (2015).
- [68] V. Vakaryuk and A. J. Leggett, *Spin Polarization of Half-Quantum Vortex in Systems with Equal Spin Pairing*, Phys. Rev. Lett. **103**, 057003 (2009).
- [69] N. Nagamura and R. Ikeda, *Stability of half-quantum vortices in equal-spin pairing states of ^3He* , Phys. Rev. B **98**, 094524 (2018).
- [70] V. P. Mineev, *Half-Quantum Vortices in Polar Phase of Superfluid ^3He* , J. Low Temp. Phys. **177**, 48 (2014).
- [71] C.-R. Hu and K. Maki, *Satellite magnetic resonances of a bound pair of half-quantum vortices in rotating superfluid $^3\text{He-A}$* , Phys. Rev. B **36**, 6871 (1987).
- [72] J. Rysti, J. T. Mäkinen, S. Autti, T. Kamppinen, G. E. Volovik, and V. B. Eltsov *Suppressing the Kibble-Zurek Mechanism by a Symmetry-Violating Bias*, Phys. Rev. Lett. **127**, 115702 (2021).
- [73] T. W. B. Kibble, *Topology of cosmic domains and strings*, J. Phys. A: Math. Gen. **9**, 1387 (1976).
- [74] W. H. Zurek, *Cosmological experiments in superfluid helium?*, Nature **317**, 505 (1985).
- [75] V. M. H. Ruutu, V. B. Eltsov, A. J. Gill, W. B. Kibble, M. Krusius, Y. G. Makhlin, B. Placais, G. E. Volovik, and W. Xu, *Vortex formation in neutron-irradiated superfluid ^3He as an analogue of cosmological defect formation*, Nature **382**, 334 (1996).
- [76] C. Bauerle, Y. M. Bunkov, S. N. Fisher, H. Godfrin, and G. R. Pickett, *Laboratory simulation of cosmic string formation in the early Universe using superfluid ^3He* , Nature **382**, 332 (1996).
- [77] Y. M. Bunkov, A. I. Golov, V. S. L’vov, A. Pomyalov, and I. Procaccia, *Evolution of a neutron-initiated micro big bang in superfluid $^3\text{He} - B$* , Phys. Rev. B **90**, 024508, (2014).
- [78] V. B. Eltsov, M. Krusius, and G. E. Volovik, *Progr. Low Temp. Phys.*, vol. XV, pp. 1–137 (Elsevier, 2005).
- [79] C. Bäuerle, Y. M. Bunkov, S. N. Fisher, H. Godfrin, and G. R. Pickett, *Superfluid ^3He Simulation of Cosmic String Creation in the Early Universe*, J. Low Temp. Phys. **110**, 13 (1998).
- [80] N. D. Mermin and T.-L. Ho, *Circulation and Angular Momentum in the A Phase of Superfluid Helium-3*, Phys. Rev. Lett. **36**, 594 (1976).
- [81] R. Blaauwgeers, V. B. Eltsov, M. Krusius, J. J. Ruohio, R. Schanen, and G. E. Volovik, *Double-*

- quantum vortex in superfluid ${}^3\text{He-A}$* , Nature **404**, 471 (2000).
- [82] J. Kasai, Y. Okamoto, K. Nishioka, T. Takagi, and Y. Sasaki, *Chiral Domain Structure in Superfluid ${}^3\text{He-A}$ Studied by Magnetic Resonance Imaging*, Phys. Rev. Lett. **120**, 205301 (2018).
- [83] M. M. Salomaa and G. E. Volovik, *Quantized vortices in superfluid ${}^3\text{He}$* , Rev. Mod. Phys. **59**, 533 (1987).
- [84] M. Silveri, T. Turunen, and E. Thuneberg, *Hard domain walls in superfluid ${}^3\text{He-B}$* , Phys. Rev. B **90**, 184513 (2014).
- [85] M. M. Salomaa and G. E. Volovik, *Cosmiclike domain walls in superfluid ${}^3\text{He-B}$: Instantons and diabolical points in (\mathbf{k}, \mathbf{r}) space*, Phys. Rev. B **37**, 9298 (1988).
- [86] M. Yamashita, A. Matsubara, R. Ishiguro, Y. Sasaki, Y. Kataoka, M. Kubota, O. Ishikawa, Y. M. Bunkov, T. Ohmi, T. Takagi, and T. Mizusaki, *Pinning of Texture and Vortices of the Rotating B-like Phase of Superfluid ${}^3\text{He}$ Confined in a 98% Aerogel*, Phys. Rev. Lett. **94**, 075301 (2005).
- [87] H. Takeuchi, *Spin-current instability at a magnetic domain wall in a ferromagnetic superfluid: A generation mechanism of eccentric fractional skyrmions*, Phys. Rev. A **105**, 013328 (2022).
- [88] M. J. Rudd, P. Senarath. Yapa, A. J. Shook, J. Maciejko and J. P. Davis, *Strong-coupling corrections to hard domain walls in superfluid ${}^3\text{He-B}$* , Phys. Rev. B **104**, 094520 (2021).
- [89] M. Nitta, *Relations among topological solitons*, Phys. Rev. D **105**, 105006 (2022).
- [90] M. Suzuki, *Group Theory I* (Springer-Verlag, 1982).
- [91] T. W. B. Kibble and G. E. Volovik, *On phase ordering behind the propagating front of a second-order transition*, JETP Lett. **65**, 102 (1997).
- [92] S. Autti, J. T. Mäkinen, J. Rysti, G. E. Volovik, V. V. Zavjalov, and V. B. Eltsov, *Exceeding the Landau speed limit with topological Bogoliubov Fermi surfaces*, Phys. Rev. Research **2**, 033013 (2020).
- [93] H. Choi, J. P. Davis, J. Pollanen, T. M. Haard, and W. P. Halperin, *Strong coupling corrections to the Ginzburg-Landau theory of superfluid ${}^3\text{He}$* , Phys. Rev. B **75**, 174503 (2007).